Gaussian process regression with levy flight optimization: Advanced AR66 adsorption studies

Intissar Harizi, Tahani Aldahri, Derradji Chebli, Hichem Tahraoui, Abdellah Bouguettoucha, Sohrab Rohani, Jie Zhang, Abdeltif Amrane

To cite this version:

Intissar Harizi, Tahani Aldahri, Derradji Chebli, Hichem Tahraoui, Abdellah Bouguettoucha, et al.. Gaussian process regression with levy flight optimization: Advanced AR66 adsorption studies. Chemical Engineering Research and Design, 2024, 207, pp.192-208. 10.1016/j.cherd.2024.05.037 . hal-04618715

HAL Id: hal-04618715
https://univ-rennes.hal.science/hal-04618715v1

Submitted on 9 Dec 2024

Gaussian Process Regression with Levy Flight Optimization: Advanced AR66 Adsorption Studies

Intissar Harizi, Tahani Aldahri, Derradji Chebli, Hichem Tahraoui, Abdellah Bouguettoucha, Sohrab Rohani, Jie Zhang, Abdeltif Amrane

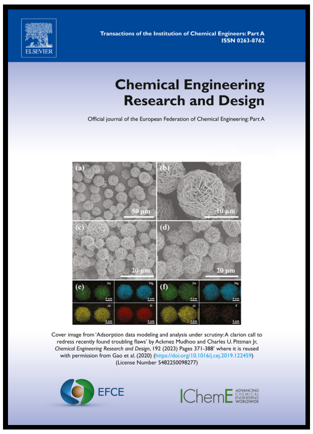

PII: S0263-8762(24)00311-3

DOI: https://doi.org/10.1016/j.cherd.2024.05.037

Reference: CHERD6315

To appear in: *Chemical Engineering Research and Design*

Received date: 25 February 2024
Revised date: 10 May 2024
Accepted date: 27 May 2024

Please cite this article as: Intissar Harizi, Tahani Aldahri, Derradji Chebli, Hichem Tahraoui, Abdellah Bouguettoucha, Sohrab Rohani, Jie Zhang and Abdeltif Amrane, Gaussian Process Regression with Levy Flight Optimization: Advanced AR66 Adsorption Studies, *Chemical Engineering Research and Design,* (2024) doi:https://doi.org/10.1016/j.cherd.2024.05.037

Gaussian Process Regression with Levy Flight Optimization: Advanced AR66 Adsorption Studies

Intissar Harizi [1,2], Tahani Aldahri [2], Derradji Chebli[1], Hichem Tahraoui [1,3,4], Abdellah Bouguettoucha [1], Sohrab Rohani [2], Jie Zhang [5], and Abdeltif Amrane [4,*]

[1] Laboratoire de Génie des Procédés Chimiques, Department of process engineering, University of Ferhat Abbas, Setif, Algeria; derradji_chebli@yahoo.fr ; hichem.tahraoui@univ-setif.dz; abd_bouguettoucha@yahoo.fr

[2] Department of Chemical and Biochemical Engineering, University of Western Ontario, London, Canada; hintissa@uwo.ca; atahani@uwo.ca; srohani@uwo.ca

[3] Laboratory of Biomaterials and Transport Phenomena (LBMPT), University of MÉDÉA, ALGERIA, Nouveau Pôle Urbain, Médéa University, 26000 Médéa, Algeria; tahraoui.hichem@univ-medea.dz

[4] Ecole Nationale Supérieure de Chimie de Rennes, CNRS, ISCR – UMR6226, Univ Rennes, 35000 Rennes, France ; abdeltif.amrane@univ-rennes1.fr

[5] School of Engineering, Merz Court, Newcastle University, Newcastle upon Tyne NE1 7RU, UK. jie.zhang@newcastle.ac.uk

Corresponding author : E-mail: abdeltif.amrane@univ-rennes1.fr; **Tel : 00 33 6 20 01 85 68 (Abdeltif Amrane)**

Abstract

The coal fly ash (CFA), which is the residue generated by coal-fired power plants, was converted into a valuable zeolite material known as zeolite P (ZNa-P) through thermal and acid pretreatments followed by microwave radiation. Various analytical techniques were utilized to analyze the resulting zeolite, including X-ray diffraction, scanning electron microscopy, Fourier transform infrared spectroscopy, thermogravimetric analysis, BET analysis, and zeta potential measurement. The efficiency of ZNa-P in eliminating anionic dyes from aqueous solutions was exhibited by successfully removing acid red dye 66 (AR66) from a solution composed of water. To optimize the removal process, Central Composite Design (CCD) was applied to investigate the impact of four main parameters: solution pH, initial dye concentration, adsorbent mass, and contact time. The generated CCD database was modeled using Gaussian process regression (GPR) with the Lévy flight distribution (LFD) optimization algorithm. The GPR model was then used to determine optimal conditions for maximum AR66 absorption (3405.3 mg/g), with a pH of 2, initial dye concentration of 1000 mg/L, adsorbent mass of 0.2 g/L, and contact time of 11 minutes. Furthermore, the GPR model exhibited significantly lower error (32.58 mg/g) in predicting the experimental values compared to the CCD model (204.92 mg/g), highlighting the efficiency and superiority of the GPR model in this study.

Graphical Abstract

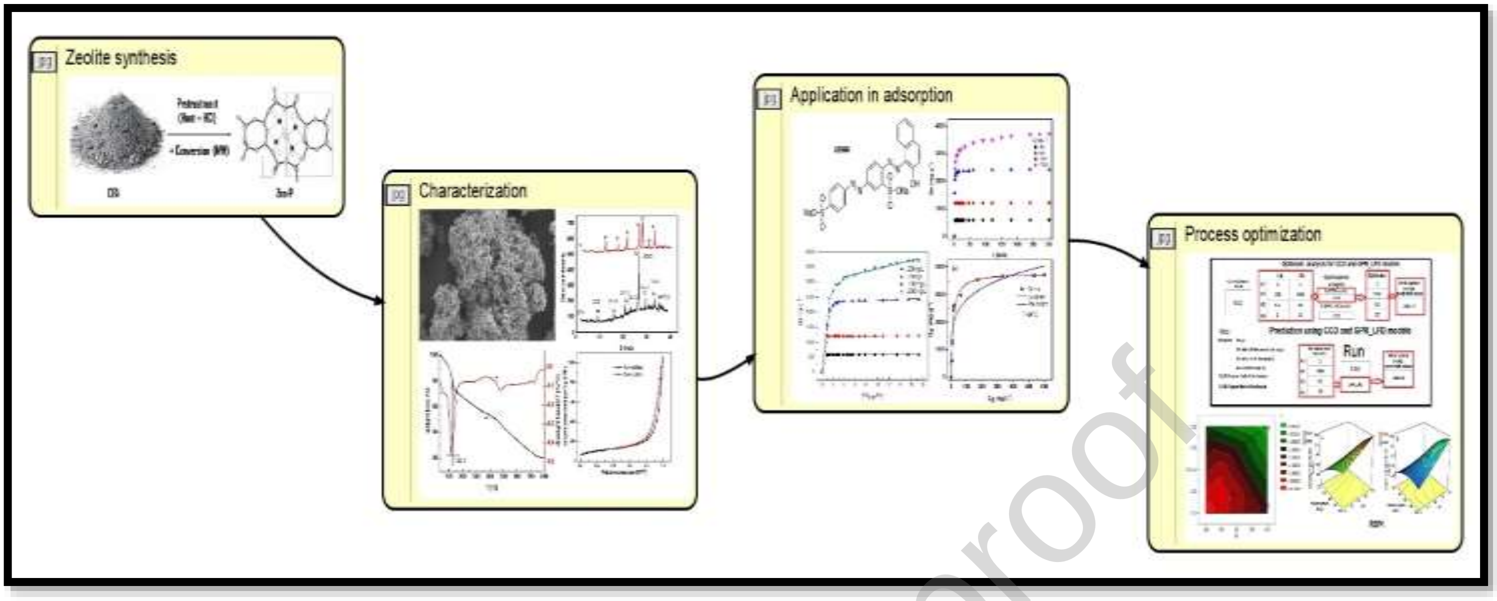

Keywords:

Acid red dye 66, Zeolite, Adsorption, Central composite design, Gaussian process regression with Lévy flight distribution.

1. Introduction

Water pollution, primarily driven by wastewater from various human activities, poses a significant threat to the environment and human well-being. [1–3] Azo dyes, widely used in industries [4] like textiles, contribute to this pollution due to their solubility, toxicity, and carcinogenicity. [5] [6] While several techniques exist for wastewater treatment, adsorption stands out for its simplicity and cost-effectiveness. [7] [8] Traditionally, activated carbon has been the preferred adsorbent, but recent studies explore alternative sorbents like calys, [9] layered double hydroxides [10], zeolites, and graphene oxides [5]. Additionally, there is a growing interest in utilizing industrial waste [11], such as coal fly ash (CFA), to synthesize eco-friendly materials for efficient dye removal [12]. Zeolites, mesoporous silica [13], and silica aerogels [14] derived from CFA show promise in this regard, highlighting the potential of waste valorization in addressing environmental challenges.

Zeolites are alumino-silicate compounds with three dimensional microporous network, formed by the interconnection of alumina and silica tetrahedra where the silicone and aluminum atoms are bonded to four and six oxygen atoms, respectively [15]. CFA is a by-product generated from the combustion of coal during the electricity production in power plants. Similarly to zeolites, coal fly ash contains high alumina and silica which make it economical and environmentally feedstock for zeolites synthesis [16]. Numerous studies have reported the successful synthesis of various types of zeolites based on raw CFA. Examples include zeolite X [17], zeolite A [18], zeolite P [19], zeolite Y [20], and chabazite [21].

The conventional synthesis methods are energy intensive, time consuming [22] and yield non-uniform, irregular and poorly crystallised zeolites [23–25]. Therefore, novel methods such as microwave assisted [26] and thermo-sonochemical conversion [27] have been developed to overcome these limitations. Aldahri et al. demonstrated that utilizing MW irradiation enhance the yield of CFA conversion and reduced the reaction time and energy consumption remarkably [28–30]. In another work, Aldahri et al. successfully synthesised different types of zeolites with distinct properties and structures using sonochemical energy [27].   Conditioning of CFA via fusion with NaOH [31] and acid treatments [22] are also realised in order to enhance the selectivity and reducibility of conversion of CFA to zeolites.

Conventionally, "one variable at a time" approach is applied to study the influence of various parameters on adsorption process by varying one parameter at a time while holding others constant [32]. A more effective approach allowing the examination of the influence of multiple factors on response systems has been developed. The Response Surface Methodology (RSM) evaluates both individual and combined effects of parameters, identifies optimal conditions, and develops mathematical models from experimental data offering valuable insights with minimal experiments.

Artificial intelligence (AI) has also been utilized in recent research to improve the optimization of the adsorption processes. AI techniques allow researchers to obtain more accurate empirical models and more effectively optimize the studies leading to more efficient and effective pollutant removal. Examples of such studies include using computational intelligence for modeling and optimization [33], studying antibiotic adsorption onto modified zeolite [34], ultrasound-assisted dye removal using amine-modified zeolitic imidazolate framework-8 [35], optimizing organic micropollutant removal with cross-linked chitosan/zeolite columns [36], developing hybrid models combining artificial neural networks (ANN) and isotherm models for ion adsorption onto zeolites [37], and optimizing ion removal from solutions using magnetic nano-zeolite through RSM and ANN [38]. These advancements integrate advanced techniques to enhance understanding, modeling, and optimization of adsorption processes for more efficient pollutant removal.

In this work, a new approach was applied to synthesize zeolite Na-P (ZNa-P) from CFA through the utilization of microwave-assisted conversion following thermal and acid pretreatments. To comprehensively assess the synthesized product, a wide array of advanced characterization techniques, including XRD, FTIR, TGA/DTA, SEM, BET analysis, and zeta potential measurements, were employed. While previous investigations have delved into the potential of zeolites as efficient adsorbents for removing diverse contaminants from water, ranging from organic compounds and heavy metals to cationic dyes, the exploration of their capacity to adsorb anionic dyes has remained relatively limited. To the best of our knowledge, this study represents a pioneering endeavor, being the first-ever reported study on the adsorption of an anionic dye, specifically Acid Red 66 (AR66), utilizing the synthesized zeolite P.

To thoroughly evaluate the adsorption of AR66 onto ZNa-P and optimize the conditions to achieve maximum dye removal efficacy, a multifaceted approach was adopted, combining both an experimental design and the sophisticated Gaussian process regression with Lévy flight distribution optimization (GPR-LFD) technique. Subsequently, the GPR-LFD model was harnessed to predict outcomes based on the comprehensive CCD database. Furthermore, an optimization process, employing the remarkable Lévy flight distribution (LFD), was meticulously conducted to identify the optimal conditions from both models. To facilitate the seamless implementation of AR66 uptake optimization and prediction, a user-friendly MATLAB Guide based application was developed, underscoring the practical significance of this study.

2. Materials and methods

2.1. Materials

In this study, the CFA utilized as a raw material for synthesizing ZNa-P was sourced from the Nanticoke generating station, a coal-fired power plant situated in Ontario, Canada. The chemicals Chlorohydric Acid and Sodium Hydroxide were obtained from Alphachem, a supplier based in Canada. The AR66 dye, selected as the pollutant for the experiments, was supplied by Alfa Aesar in Canada. AR66 is an azo dye commonly employed in various industrial applications and exhibits high solubility in water. Its chemical formula is $C_{22}H_{14}N_4O_7S_2Na_2$, and it has a molecular weight. The dye has a maximum wavelength (λmax) of 506 ± 4nm. Figure 1 depicts the molecular composition of AR66.

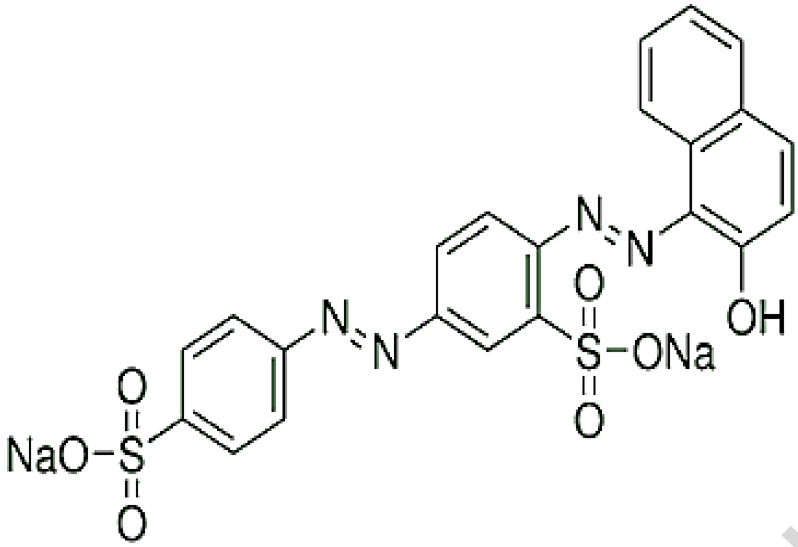

Figure 1. Molecular formula of Acid Red 66

2.2. Adsorbent synthesis procedure

In this study, the preparation of ZNa-P involved a three-step procedure. Firstly, a weighed mass of the raw CFA was subjected to a thermal treatment. The CFA was sieved through a 600µm screen and then placed in a Lindberg Blue M Box furnace at a temperature of 800°C for 1 hour. Following the thermal treatment, the calcined CFA was acidly treated using a 0.1M HCl solution. Specifically, 2g of the calcined CFA was mixed with 20ml of the HCl solution. The mixture was stirred slowly for 3 hours at a temperature of 65°C. The solid was subsequently recovered by filtration, washed with deionized water, and dried at 60°C to prepare it for the conversion into zeolite. The dried solid obtained from the previous step was then combined with a 1M NaOH alkaline solution. The combination was inserted into a Teflon tube and subsequently placed inside a microwave apparatus (single-mode, 2.5 GHz, CEM cooperation, Discover, USA). The microwave operated under total reflux conditions, atmospheric pressure, and an adjusted radiation power of 250W for 45 minutes. Following the hydrothermal treatment facilitated by the microwave, the tube was cooled down, and its contents were filtered. The solid material obtained from the filtration was rinsed with deionized water and allowed to air-dry overnight at room temperature. The resulting powder was then stored for future utilization in subsequent experiments.

2.3. Characterization

In this research, several analytical techniques were employed to characterize the raw CFA and the prepared zeolite. The elemental composition of the original CFA was analyzed using wavelength dispersive X-ray fluorescence analysis. The analysis was performed using a Panalytical PW2400 spectrometer. The XRD data for both the initial CFA sample and the synthesized zeolite were acquired using a Rigaku-Mini-Flex powder diffractometer from Japan. The XRD measurements were conducted in the 2θ range of 0° to 40°, with Cu (Kα) radiation ($\lambda = 1.54059$ Ǻ). FTIR spectra of the zeolite before and after adsorption were collected using a Bruker vector 22 spectrometer. Surface imaging of both the original CFA and the zeolite was conducted using a Hitachi S-3000N scanning electron microscope (SEM) from Joel, Japan. The spectra were recorded within the wavenumber range of 400 to 4000 cm^{-1}. The SEM analysis was carried out at an acceleration voltage of 10 keV. TGA/DTA analysis of the zeolite was carried out using a Mettler Toledo analyzer (model 851e, Switzerland) with Stare software version 6.1. The measurements involved subjecting a weighed mass of the zeolite to a temperature range of ambient to 600°C, under a nitrogen purge of 30 mL/min, with a heating rate of 10°C/min. The point of zero charge (pHzc) of the zeolite was determined by measuring the zeta potential at different pH values. Fixed amounts of zeolite particles were dispersed in 20 mL of aqueous solutions with varying pH. The zeta potential of each suspension was analyzed using a Malvern ZetaSizer 3000 instrument from the UK. The pHZC, which corresponds to the pH value at which the zeta potential is zero, was determined. These characterization techniques provided valuable information regarding the elemental composition, crystal structure, surface morphology, thermal behavior, and surface charge properties of both the original CFA and the synthesized zeolite.

2.4. Adsorption experiments

In the batch mode adsorption experiments, a specified mass of the adsorbent (0.2-0.5 g/L) was introduced into 50 mL of a dye solution with a known concentration (200-1000 mg/L) and controlled pH (2-4). The experiments were carried out using a magnetic stirrer operating at a constant speed of 200 rpm. The adsorption process was allowed to take place for a designated contact time (5-25 min). After reaching the desired time, the solution was subjected to centrifugation in order to separate the solid adsorbent from the liquid phase, thereby stopping the adsorption process. All experiments were performed at room temperature (approximately 24±1°C), unless the effect of temperature was being investigated. For the kinetic studies, a fixed mass of 80 mg of ZNa-P was placed in contact with 200 mL of the dye solution. The mixture was stirred magnetically at 200 rpm and at room temperature. Samples (1 mL) were taken at regular intervals until equilibrium was established, allowing for the determination of the adsorption kinetics. Adsorption isotherms were investigated by adding 20 mg of ZNa-P to 50 mL of dye solutions with varying initial concentrations (50-2000 mg/L). The experiments were conducted at room temperature with a fixed stirring speed of 200 rpm. Thermodynamic studies of adsorption were performed by examining the effect of temperature (10-40°C). A mixture of 50 mL of dye solution (1000 mg/L) and 20 mg of ZNa-P was stirred on a magnetic stirrer equipped with a thermostat to maintain the desired temperature.

The residual dye concentration after adsorption was determined by analyzing the supernatant of the centrifuged samples using a Shimadzu UV spectrometer (model 1601) at the wavelength λmax=506±2 [39]. The capacity of adsorption Q_t (mg/g) and the removal percentage η (%) were calculated by using Equations 1 and 2 respectively [40]. In the context of the experiment, the variables C_0, C_t, and C_e represent the initial dye concentration, the concentration at time t minutes, and the dye concentration at equilibrium respectively [40]. The variable V denotes the volume of the dye solution (in liters), and m represents the mass of the adsorbent (in grams) that was brought into contact with the dye solution [40–44].

$$Q_t(mg/g) = \frac{C_0 - C_t}{m} * V \qquad \text{Eq. 1}$$

$$\eta(\%) = \frac{C_0 - C_e}{C_0} * 100 \qquad \text{Eq. 2}$$

2.5. Experimental design

In the study, the JMP Pro 13 software was utilized to perform a design of experiment (DOE) for the adsorption of AR66 onto ZNa-P. The RSM design chosen for this study was the CCD. The CCD design incorporates five variation levels (-α, -1, 0, 1, and +α) for each independent experimental factor [45–48]. For a total of n experimental factors, the CCD consists of a specific number of experiments, denoted as N. To calculate the total number of experiments, Equation 3 can be used [40], divided in three series of points [49]: 2^n factorial points, 2n axial points and 6 replicated center points.

$$N = 2^n + 2n + 6 \qquad \text{Eq.3}$$

In this study, as shown in Table 1, four input variables were selected for the adsorption process: the initial pH of the solution (ranging from 2 to 4), the initial concentration of the dye solution (C_0, ranging from 200 to 1000 mg/L), the adsorbent dosage (m, ranging from 0.2 to 0.6 mg/g), and the contact time (t, ranging from 5 to 25 minutes). These variables were assigned coded values, denoted as X_1, X_2, X_3, and X_4, respectively.

The response variable (Y) of interest in this study was the adsorption capacity (mg/g) of the dye on ZNa-P. The aim was to optimize this response, i.e., maximize the adsorption capacity, by studying and analyzing the effects of the independent variables.

The CCD was employed in this study to establish a regression model between the response variable (Y) and the independent variables (X_1, X_2, X_3, and X_4). By conducting a series of experiments based on the CCD, the relationship between the response and the independent variables can be determined and a regression equation can be developed to describe this relationship. The regression equation obtained through the CCD enables the prediction and optimization of the adsorption capacity based on the specified ranges of the independent variables. The key factors and their effects on the adsorption process can be identified by analyzing the regression coefficients and the significance of the model terms. This information is valuable for understanding the adsorption mechanism and for optimizing the process conditions to achieve the maximum adsorption capacity of the dye on ZNa-P.

Table 1. The independent variables and their coded levels using CCD

Factor	- 2 Level	-1 Level	0 Level	+1 Level	+ 2 Level
X_1: pH	2	2.5	3	3.5	4
X_2: C_0 (mg/L)	200	400	600	800	1000
X_3: m (g/L)	0.2	0.3	0.4	0.5	0.6
X_4: t (min)	5	10	15	20	25

2.6. Kinetics models

2.6.1 Pseudo first order kinetic model

The Lagergren and Svenska [50] pseudo-first-order kinetic model has been extensively employed for predicting sorption kinetics. According to this model, the sorption rate of the pollutant onto the adsorbent is directly proportional to the amount of pollutant adsorbed from the solution phase.

$$\frac{dQ_t}{dt} = k_1(Q_e - Q_t) \quad \text{Eq. 4}$$

In this equation, the parameter k_1 (expressed in minutes^{-1}) represents the rate constant associated with pseudo-first-order adsorption, the parameter Q_e corresponds to the quantity of dye that is adsorbed at the point of equilibrium, and Q_t represents the quantity of dye adsorbed at a given time, t, measured in milligrams per gram (mg/g). By integrating Equation 4 and applying the boundary conditions of $Q_t = 0$ at $t=0$ and $Q_t = Q_e$ at $t=\infty$, we can derive the expression for Q_t.

$$Q_t = Q_e(1 - e^{-k_1 t}) \quad \text{Eq. 5}$$

After the process of linearization and simplification, Equation 5 is transformed into its simplified form.

$$ln(Q_e - Q_t) = ln\, Q_e - k_1 t \quad \text{Eq.6}$$

A linear correlation is observed when plotting the natural logarithm of (Q_e- Q_t) against time (t). This linear relationship facilitates the straightforward calculation of the rate constant (k_l) by analyzing the slope of the line, while the equilibrium adsorption capacity (Q_e) can be determined by examining the intercept at t=0.

2.6.2. Pseudo-second-order model

The sorption process of pollutants onto adsorbents is often described using the modified pseudo-second-order kinetic equation. This widely utilized model, denoted as Equation 7, is commonly employed in various studies focusing on this subject matter [51,52],

$$\frac{dQ_t}{dt} = k_2(Q_e - Q_t)^2 \quad \text{Eq. 7}$$

Again Q_t (mg/g) and Q_e (mg/g) represent the amount of adsorbed pollutant at a specific time, t (min), and at equilibrium, respectively, and play a significant role in the characterization of the pseudo-second-order kinetic model. . The rate constant for the pseudo-second-order process is denoted as k_2 (g/mg•min). By taking into account the boundary conditions of $Q_t = 0$ at t = 0 and

$Q_t = Q_e$ at $t = \infty$, integrating, and rearranging Equation 7, we can derive the expression for Q_t within this model as follows:

$$\frac{t}{Q_t} = \frac{1}{k_2 Q_e^2} + \frac{t}{Q_e} \qquad \text{Eq. 8}$$

The initial rate of sorption is determined at t=0 and can be calculated using the following equation (Eq.9).

$$h = k_2 Q^2 \qquad \text{Eq. 9}$$

When the kinetics data conform well to this model, plotting t/Q_t against t will yield linear graphs characterized by a slope of $1/Q_e$ and an intercept of $1/h$.

2.6.3. Elovich model

The Elovich Model or Roginsky-Zeldovich equation [53] is commonly employed to investigate the kinetics of chemisorption capacity between a pollutant and an adsorbate [54]. In general, the Elovich model describing the adsorption capacity is shown in Eq. 10 [55,56].

$$Q_t = \frac{1}{\beta}\ln(\alpha.\beta) + \frac{1}{\beta}\ln(t) \qquad \text{Eq. 10}$$

where Q_t (mg/g) denotes the amount of pollutant adsorbed at a given time t (min), the parameter α (mg/g.min) indicates the initial rate of pollutant adsorption, and β (g/mg) represents the desorption constant.

2.6.4. Diffusion-chemisorption model

An alternative method for describing the adsorption process of dyes on adsorbents is the diffusion-chemisorption model developed by Sutherland and Venkobachar [57]. This model is given in Equation 11.

$$\frac{t^{0.5}}{Q_t} = \frac{1}{k_{DC}} + \frac{1}{Q_e} t^{0.5}$$ Eq. 11

The diffusion-chemisorption constant, denoted as k_{DC} (mg/g.min$^{1/2}$), plays a significant role in the equation.

By creating a plot of $t^{0.5}/Q_t$ against $t^{0.5}$, the diffusion-chemisorption model can be constructed for the adsorption process of AR66 on ZNa-P. Sutherland and Venkobachar discovered that the initial slope of the experimental kinetic curve corresponds to both k_{DC} and Q_e. To approximate a linear region as t approaches zero, Sutherland and Venkobachar proposed the following empirical relationship (Eq. 12)[57].

$$k_i = k_{DC}^2 / Q_e$$ Eq. 12

where k_i (mg/gmin) is the initial sorption rate.

1.1.5. Intra-particle diffusion model

The kinetics of adsorption play a crucial role in describing the process of solute adsorption onto an adsorbent and the mechanism of adsorption diffusion is commonly described by the intra-particle diffusion model. In this study, the adsorption kinetics experimental results were utilized to investigate the diffusion mechanism of AR66 adsorption on ZNa-P. Consequently, the model parameters obtained can be employed to forecast the rate of dye adsorption. The equation representing the intra-particle diffusion model, known as the Weber-Morris equation (Eq.13) [58], is used for this purpose.

$$Q_t = k_{id} t^{0.5} + C$$ Eq. 13

The intra-particle diffusion model is defined by two key parameters: the rate constant k_{id} (mg/g.min$^{1/2}$) and the intercept C. These parameters offer valuable information regarding the thickness of the boundary layer.

2.7. Isotherms models

Equilibrium studies, which involve adsorption isotherms, play a crucial role in understanding adsorption processes. They provide insights into the interaction between the adsorbent and adsorbate, as well as the maximum adsorption capacity. Various models, including the Langmuir and Freundlich models (two-parameter models) and the Sips and Toth models (three-parameter models), are commonly employed to analyze equilibrium data.

2.7.1. Langmuir model

Langmuir non-linearized equation is given by Equation.14 [59].

$$\frac{Q_e}{Q_m} = \frac{K_L C_e}{1+K_L C_e} \qquad \text{Eq. 14}$$

In the Langmuir adsorption isotherm model, the Langmuir adsorption constant, K_L (expressed in L/mg), reflects the energy of adsorption providing insights into how strongly the adsorbate interacts with the adsorbent surface. Q_e (in mg/g) signifies the equilibrium adsorption capacity representing the amount of dye adsorbed at the point of equilibrium. Q_m (in mg/g) represents the maximum capacity of the adsorbent's monolayer signifying the maximum amount of dye that can be adsorbed by the adsorbent per unit mass. C_e (in mg/L) indicates the dye concentration at equilibrium, which corresponds to the dye concentration remaining in the solution phase after the adsorption process has reached equilibrium.

In order to evaluate the viability of the adsorption process, the Langmuir model incorporates a significant parameter known as the separation factor R_L. This factor is instrumental in determining the favorability of the adsorption process. R_L values ranging from 0 to 1 signify favorable adsorption, $R_L = 0$ indicates irreversible adsorption, $R_L = 1$ suggests a linear relationship, and RL values greater than 1 indicate unfavorable adsorption. The R_L expression is given by Eq.15 [60].

$$R_L = \frac{1}{1+K_L C_0} \qquad \text{Eq. 45}$$

The Langmuir constant, denoted as K_L, and the highest initial concentration, represented as C_0, are key components in this model.

2.7.2. Freundlich model

The nonlinear equation for the Freundlich model can be expressed as follows (Eq.16) [59].

$$Q_e = K_F C_e^{1/n} \qquad \text{Eq. 56}$$

The above equation involves empirical constants, K_F (L/mg) and *n*, which symbolize the sorption capacity and sorption intensity, respectively. Q_e (mg/g) signifies the adsorption capacity at equilibrium, while C_e (mg/L) denotes the dye concentration at equilibrium.

2.7.3. Sips model

The Sips model is a hybrid of the Langmuir and Freundlich isotherms, providing a comprehensive description of adsorption. It can be mathematically represented by Eq.17.[59]:

$$\frac{Q_e}{Q_m} = \frac{(K_S C_e)^m}{1+(K_S C_e)^m} \qquad \text{Eq. 67}$$

The Sips model incorporates the adsorption energy and intensity and is characterized by the constant K_S (L/mgm) and the exponent m. These parameters govern the adsorption behavior according to the Sips model.

2.7.4 Toth model

The Toth model, an adaptation of the Langmuir model, can be mathematically expressed using the following equation (Eq.18) [61]:

$$q_e = \frac{K_T C_e}{[a_T + C_e]^{1/t}} \qquad \text{Eq. 78}$$

The parameters for the various models were determined by employing non-linear regression and fitting the isotherm data to the models using Origin software. Through this analysis, the constants of each model, including K_T (mg/g), a_T (L/mg), and t, were obtained.

2.8. Gaussian Process Regression coupled with Lévy flight distribution

This article elucidates the concept of Gaussian process regression (GPR) as a statistical technique comprising a sequence of random variables that demonstrate a collective Gaussian distribution when constrained within a particular interval. This illustrative approach can be employed effectively for tasks involving regression as well as classification [40,47,62].

GPR denotes a collection of random variables assumed to possess a joint Gaussian distribution when considered in any finite number. This characteristic distinguishes GPR as a statistical framework suitable for various applications, including regression and classification tasks. *[40,47,62]*. GPR encompasses the representation of an unknown function f(x) by means of its mean function, m(x) = E [f(x)], and a kernel function, k(x, x′), which estimates the covariance, E [(f(x) − m(x))(f(x′) − m(x′))]. The kernel function, acting as a measure of geometrical distance, indicates that inputs in close proximity exhibit a stronger correlation in terms of their respective function values. This enables GPR to capture and model the underlying relationships between data points based on their spatial arrangement *[40,47,62]*. GPR relies on a covariance function, often referred to as a kernel, to characterize the structure of the target function. The selection of the kernel function and its associated parameters plays a crucial role in determining the representativeness and accuracy of the GPR model, given that different kernel functions can be employed. The choice of kernel function should align with the specific characteristics and patterns present in the data, allowing the GPR model to effectively capture and model the underlying relationships *[40,47,62]*.

This study utilized GPR to predict the adsorbent uptake. The GPR model was built using data obtained from the design of the experiment. To enhance the GPR model's accuracy, a kernel and parameter optimization technique was employed. The development of the model involved a series of steps aimed at optimizing the performance of GPR and refining its predictive capabilities *[40,47,62]*. The development of the GPR model for predicting the adsorbent amount involved the following steps:

1. Normalization: Each variable in the database was normalized to the range of [-1, +1]. This normalization process ensures that variables are on a consistent scale and facilitates accurate model training.

2. Data Split: The database was divided into two parts: 70% for training the GPR model and 30% for validation. This partitioning allows for model evaluation and assessment of its predictive performance.

3. Kernel Optimization: Ten different kernel functions, including exponential, exponential squared, matern32, matern52, quadratic rational, ard exponential, ard exponential squared, ardmatern32, ardmatern52, and ard quadratic rational, were optimized. The optimization process involved exploring various basis functions (constant, linear, PureQuadratic, and zero) and fine-tuning the parameters (Kernel Scale [sigmaM, sigmaF] and sigma) of each kernel function. To date, manual optimization is a significant drawback due to the considerable time it takes to find the optimal model. In order to enhance the efficiency of the prediction model and achieve superior outcomes,

optimization algorithms have been employed *[63]*. Optimization algorithms have demonstrated their effectiveness in addressing a wide range of optimization problems, encompassing areas such as machine learning, value optimization, and penalty setting. These algorithms have been shown to be valuable tools in finding optimal solutions and improving the overall performance of the systems involved *[64]*. A multitude of studies have provided evidence that employing optimization algorithms to optimize hyper-parameters in machine learning algorithms results in enhanced performance. These algorithms effectively search the hyper-parameter space, enabling the discovery of optimal configurations that maximize the model accuracy or minimize the model error. By fine-tuning the hyper-parameters, the machine learning algorithms can better adapt to the data and produce more accurate predictions or classifications. This approach has been widely adopted in the field of machine learning to achieve improved results across various tasks and datasets *[40,47,63–66]*.

In this particular study, the authors introduced a novel approach called GPR_LFD, which combines the Levy Flight Distribution (LFD) algorithm with GPR to optimize the parameters of each kernel function. This approach, first introduced in 2021 by Houssein et al. *[63]*, aims to enhance the optimization process by leveraging the exploration capabilities of the LFD algorithm and the regression capabilities of GPR. By integrating these two techniques, the authors aim to improve the efficiency and accuracy of parameter optimization in the context of kernel functions.

2.9. Statistical evaluation criteria

In the present study, the quality of the CCD was evaluated using analysis of variance (ANOVA) [40,47]. The fitting quality of the CCD was assessed using coefficient of determination R^2 and adjusted R^2 [40,47]. The statistical significance of the model was determined through the calculated F-value (Fisher variation ratio) and P-value (probability) [40,47]. The individual factors and their interactions were evaluated by analyzing the P-value for each term [40,42,47]. Furthermore, the relationship between the response and variables was visually represented through 2D and 3D plots using the root mean square error (RMSE) [40,47].

The performance of each GPR model was evaluated using various performance measures including the correlation coefficient (R), R^2, R^2_{adj} (adjusted R^2), RMSE, mean absolute error (MAE), Error Standard of Prediction (ESP), and Error Prediction of Model (EPM). The equations for calculating these parameters were provided in the works [48,49,67–74,74–76].

$$R=\frac{\sum_{i=1}^{N}\left(y_{\exp}-\overline{y}_{\exp}\right)\left(y_{pred}-\overline{y}_{pred}\right)}{\sqrt{\sum_{i=1}^{N}\left(y_{\exp}-\overline{y}_{\exp}\right)^2\sum_{i=1}^{N}\left(y_{pred}-\overline{y}_{pred}\right)^2}} \tag*{\textit{Eq.19}}$$

$$R^2_{adj}=1-\frac{\left(1-R^2\right)\left(N-1\right)}{N-K-1} \tag*{\textit{Eq.20}}$$

$$RMSE=\sqrt{\left(\frac{1}{N}\right)\left(\sum_{i=1}^{N}\left[\left(y_{\exp}-y_{pred}\right)\right]^2\right)}$$

Eq.21

$$MAE=\left(\frac{1}{N}\right)\sum_{i=1}^{N}\left|y_{\exp}-y_{pred}\right| \tag*{\textit{Eq.22}}$$

$$ESP\left(\%\right)=\frac{RMSE}{\overline{y_{\exp}}}\times 100 \tag*{\textit{Eq.23}}$$

$$EPM\left(\%\right)=\frac{100}{N}\sum_{i=1}^{N}\left|\frac{\left(y_{\exp}-y_{\mathrm{pred}}\right)}{y_{\exp}}\right| \tag*{\textit{Eq.24}}$$

In the above equations, *N* is the number of data samples, *K* is the number of input variables, $y_{\exp}$ and y_{pred} are the experimental and the predicted values respectively, $\bar{y}_{\exp}$ and $\bar{y}_{pred}$ are respectively the average values of the experimental and the predicted values [77–82].

3. Results and discussion

The XRD patterns of the raw CFA and the synthesized ZNa-P were collected and presented in Figure 2. It can be observed that the raw CFA mainly consists of the crystalline phases: quartz (Q), mullite (M) , hematite (H), and calcite (C). A clear distinction can be seen when comparing the XRD patterns of the raw CFA with the resulting product. In XRD pattern for CFA, peaks corresponding to crystalline phases M and C at 2θ = 9.4° and 29.54°, respectivaly, disappeared from that for the synthesized ZNa-P. This phenomenen is attributted to the complete dissolution of the calcite and mullite phases leading to the form of zeolitic phases. However, a noticeable decrease in the intensity of the main peak assotiated with the quartz phase in the CFA, observed at 26.77°, suggests the partial dissolution of the quartz phase. Simultaneously, new sharp peaks caracteristic of zeolite crystalline phases at 2θ = 12.68°, 17.78°, and 28.26° became evident confirming the formation of well critallined zeolitic material. Consequently, at least three characteristic peaks appeared at 2θ = 12.68°, 17.78°, 21.86°, 28.26°, 31.08°, and 33.56° confirming the successful zeolitisation process. Through cross-referencing the XRD pattern of CFA post-conversion with the zeolite database [27], the zeolite material was identified as ZNa-P.

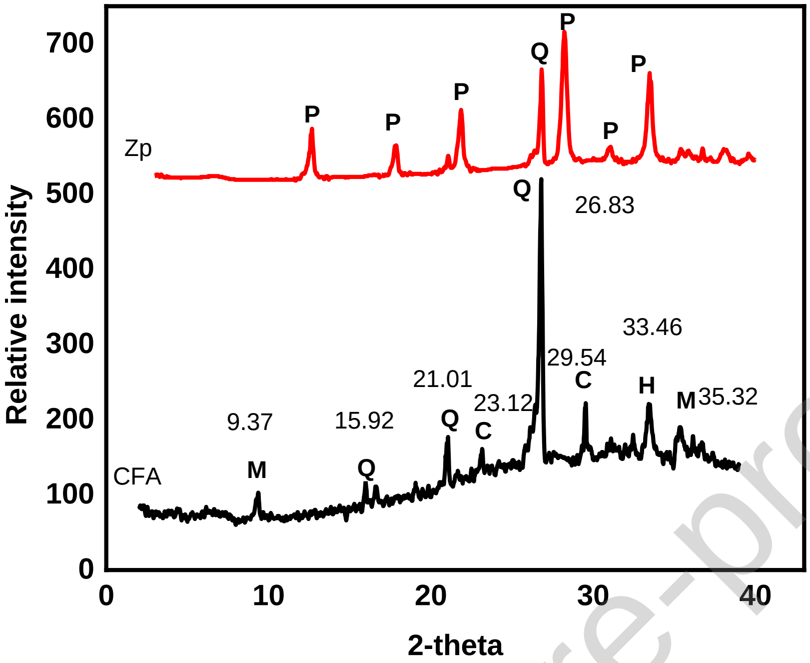

Figure 2. XRD patterns of the raw CFA and the synthesized ZNa-P

Figure 3 presents the SEM images for the raw CFA and the ZNa-P. The SEM image of the CFA reveal smooth, spherical particles of varying sizes, whereas that of ZNa-P reveals a rough surface with uniformly scattered protrusions. These alterations in surface morphology provide compelling evidence for the formation of zeolitic substances, as corroborated by the XRD patterns. The structure of the ZNa-P derived from the conversion of CFA (Figure 3) comprises polycrystals composed of small plate-like structures, exhibiting a pseudo-spherical appearance when observed under SEM [83].

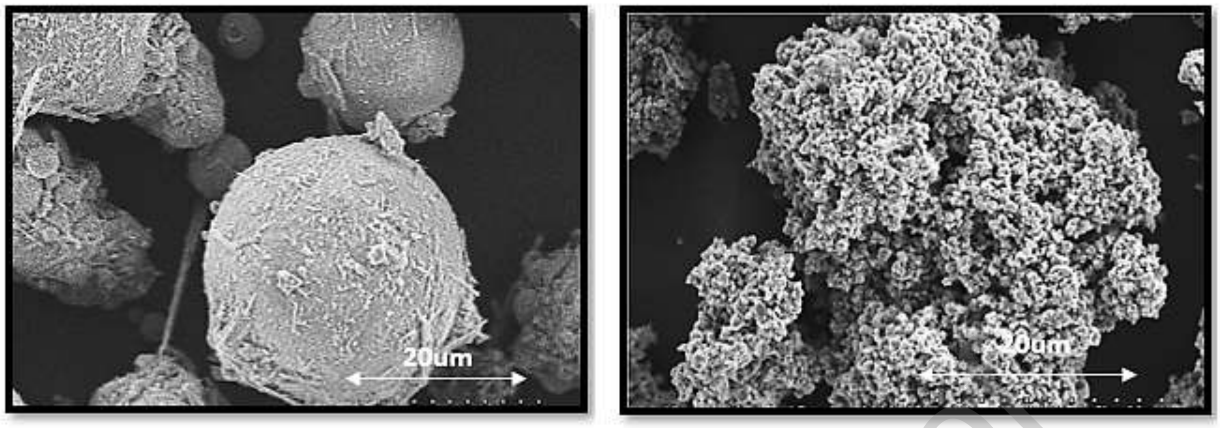

(a) (b)

Figure 1. SEM images of (a) CFA and (b) ZNa-P

Figure 4 illustrates the FT-IR spectra of the raw CFA and ZNa-P before and after dye adsorption. A comparison of the peaks observed in the FT-IR spectrum of ZNa-P with that of the raw CFA indicates the successful conversion of CFA, as previously confirmed by the XRD results. The specific peaks of ZNa-P align with those reported by Flanigen et al. [84]. The primary vibration peak at 973 cm^{-1} corresponds to the asymmetric stretching of internal tetrahedral $SiO^{4/2}$ and $AlO^{4/2}$ [85]. The double ring external linkage vibration produces a peak at 563 cm^{-1}. Peaks at 668 cm^{-1} and 740 cm^{-1} can be attributed to the internal and external tetrahedral symmetrical vibrations of Si-O and Al-O respectively. The peak at 1646 cm^{-1} and the weak but broad peak at 3412 cm^{-1} are associated with the H-O-H bending of the adsorbed water molecules. It is evident that the adsorption of the dye onto ZNa-P does not induce significant changes in the FT-IR pattern. This can be attributed to weak signals, low dye concentration, or overlap of the primary absorbance peaks of the dye with those of ZNa-P. Similar observations were reported by Humelnicu et al. [15].

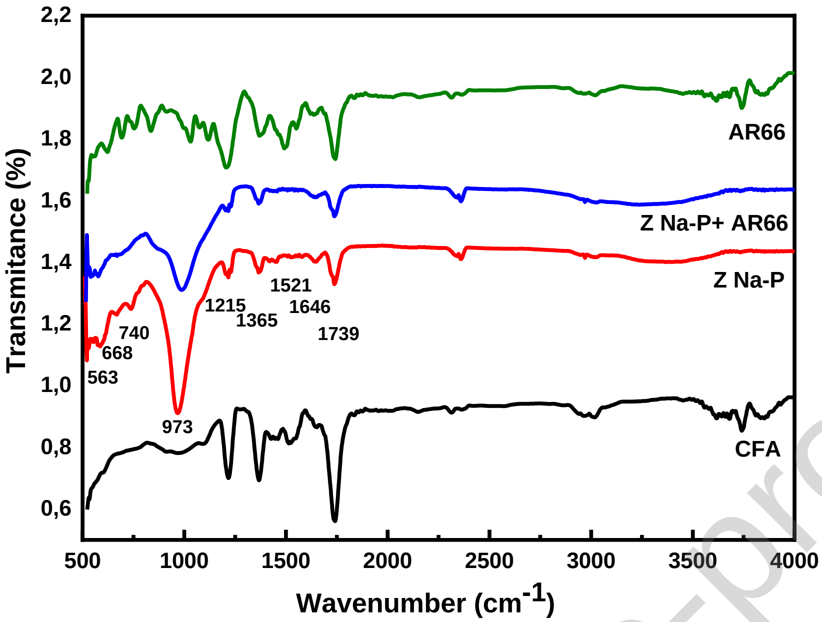

Figure 4. FTIR spectra of a raw CFA, ZNa-P, ZNa-P + AR66 and AR66

The thermal stability of ZNa-P was investigated through thermal analysis, specifically thermogravimetric analysis (TGA) and differential thermogravimetric analysis (DTA). The results of these analyses are presented in Figure 5. Within the temperature range of 23°C to 800°C, ZNa-P exhibited a loss of approximately 20% of its initial weight, whereas the raw CFA only recorded a 5% weight loss. This indicates the superior water-holding capacity of ZNa-P compared to CFA. The TGA results reveal that ZNa-P experienced weight loss in three distinct steps, as supported by the presence of three peaks in the DTA curve. The first step, observed at low temperatures (T < 130°), can be attributed mainly to the elimination of physically adsorbed water from zeolite surface. The weight loss in the second stage is assigned to the removal of chemically adsorbed water and the decomposition of the hydroxyl groups within zeolite network. Further weight loss occurs at higher temperature, which may indicate the decomposition of organic and inorganic impurities within zeolite structure, or possibly to the collapse of the zeolite framework caused by thermal degradation.

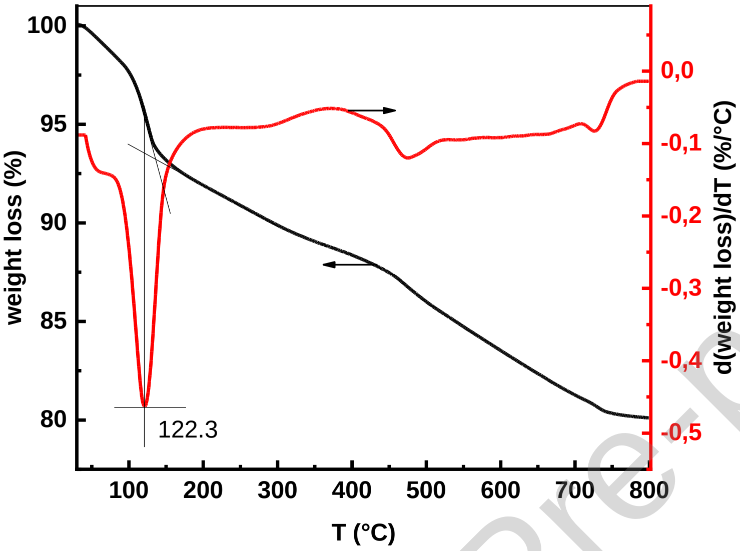

Figure 5. TGA and DTA curves of ZNa-P (heating rate =10 ◦C min^{-1}, under 40 mLmin^{-1} N_2*)*

The results of nitrogen adsorption-desorption are presented in Figure 6 and the structural properties are displayed in Table 2. The specific surface area of ZNa-P was determined to be 378 m^2/g, which is significantly higher than that of the raw CFA at approximately 15.47 m^2/g. This indicates that the synthesis method employed in this study enables the production of a product with a surface area approximately 24 times larger than that of the initial raw material. The pore volume of ZNa-P was measured at 1.63 cm^3/g, with a pore size of 199.65Å. In the structure of zeolites, tetrahedral units comprising Si and Al atoms are surrounded by four oxygen atoms. As the Si-O and Al-O units do not completely occupy the available space, the resulting cavities contribute to increased porosity and a higher surface area. The structural properties of ZNa-P, synthesized through heat and acid treatments of the CFA, were found to exceed those of zeolites

P obtained through other methods, such as the conventional method [30] or through acid treatment alone [86].

Table 2. Textural properties of ZNa-P

Surface area (m^2/g)	Pore size (Å)	Pore volume (cm^3/g)
378.0655	199.6553	1.6306

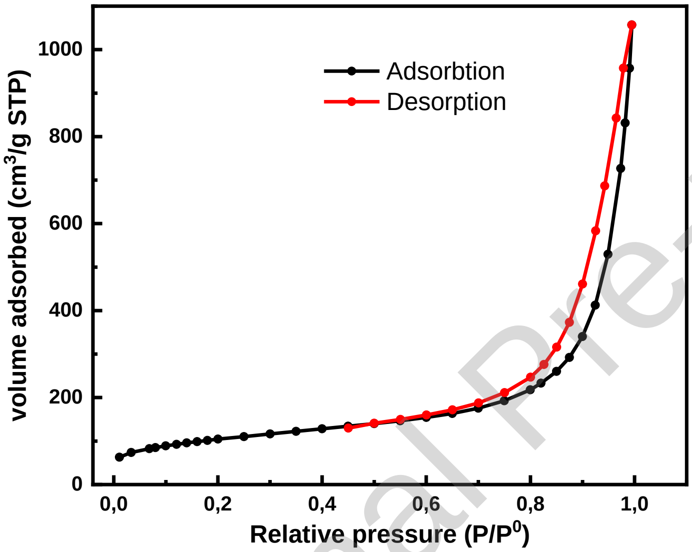

Figure 6. N_2 adsorption desorption isotherms of ZNa-P

3.2. CCD regression model development

The experimental design matrix, utilizing the central composite design (CCD) performed by JMP Pro 13 software, and the outcomes of the quadratic response are presented in Table A1 in the appendix. The experimental design encompassed a total of 30 experimental runs, including 6 central replicates positioned at the zero level (0,0,0,0) for the parameter values. The results demonstrate that the adsorption capacity (response) exhibited considerable variations across the different levels of the factors.

3.3. Investigation of variables effects

The impacts of the different variables on the dye adsorption capacity of ZNa-P are illustrated in 2D contour and 3D response surface generated by the design software (Figure 7). The pH of the solution was found to have a profound influence on the adsorption capacity, as depicted in Figure 7 (a, b and c). The highest adsorption capacities of AR66 on ZNa-P, represented by the red surfaces, were observed at lower pH values. As the pH increased, the adsorption capacity gradually decreased, reaching its lowest values at higher pH levels, represented by the blue area. This behavior can be attributed to the electrostatic forces between the ionized dye molecules in the aqueous solution and the charges acquired by the adsorbent surface at different pH values. Further insights into this phenomenon can be obtained by studying the zeta potential of ZNa-P with the results presented in Table 3. The zeta potential decreased with increasing pH and the point of zero charge (pHzc) of ZNa-P was observed at pH 5.37. Consequently, at a pH lower than pHzc, the ZNa-P surface carries a positive charge due to protonation, while at a pH higher than pHzc, the surface undergoes deprotonation and acquires a negative charge. The decrease in zeta potential and, consequently, the reduction in positive charges can adequately explain the decrease in adsorption capacity for negatively charged molecules. It is noteworthy that even at a pH value of 4, the adsorption capacities remained remarkably high, surpassing 1000 mg/g. The individual effect of pH was particularly significant, as indicated by the high F-value of 225 obtained through ANOVA analysis for this parameter.

Table 3. Zeta potential of ZNa-P at different pH

pH	**Zeta potential**
2	23.65
4	15.27
6	-5.71
8	-16.85

10	-19.48
12	-25.14

The influence of the initial concentration on the adsorption capacity of AR66 is clearly demonstrated in Figure 7 (a and d). A higher initial concentration corresponds to a greater adsorption capacity due to the increased likelihood of interaction between the dye and the adsorbent. This leads to the adsorption of more dye molecules, effectively utilizing a larger portion of the adsorbent's active surface [87]. The ANOVA results corroborate the significant impact of the initial dye concentration, as evidenced by the highest F-value of 832.22, indicating its strong influence on the adsorption capacity. Similarly, the mass of the adsorbent is identified as another important factor affecting the adsorption capacity, as indicated by an F-value of 442.34. The utilization of a smaller mass of adsorbent significantly enhances the adsorption capacity, as it is calculated per unit of mass. In other words, adsorbing the same amount of dye on a larger surface area (resulting from a larger adsorbent mass) reduces the adsorption capacity, whereas a smaller adsorbent mass is sufficient to achieve the same dye removal. An adsorbent dosage of 0.2 g/L has been shown to be effective, resulting in a high adsorption capacity, surpassing 3000 mg/g under specific conditions.

The impact of contact time on the adsorption capacity is also depicted in Figure 7 (c and d), revealing that longer contact times lead to higher adsorption capacities. However, compared to the other factors, the effect of contact time on the adsorption capacity is relatively less significant, as indicated by the lowest F-value of 41.83 and the slightly upward sloping contour curves of the adsorption capacities.

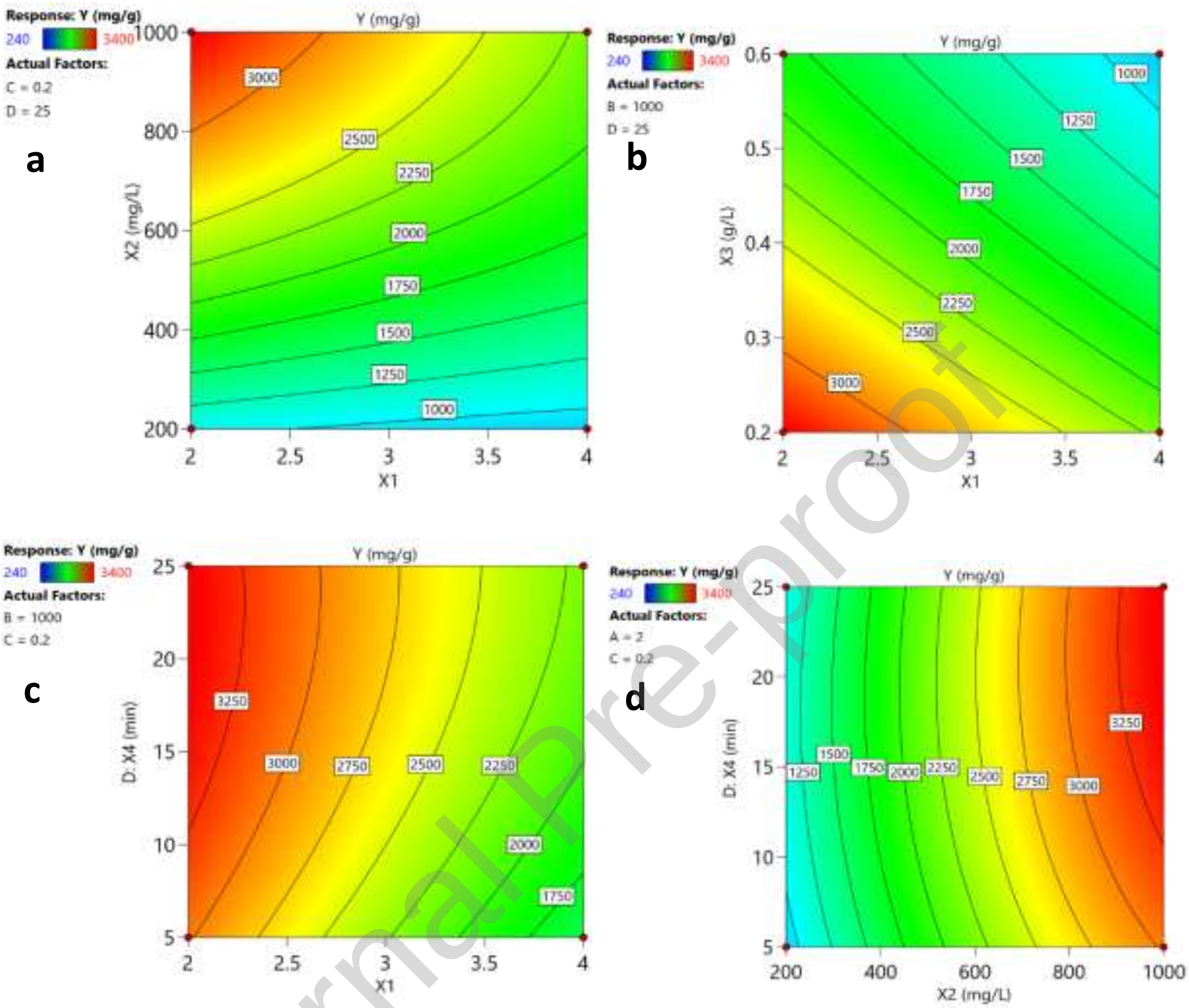

Figure 7. 2D response surface plots for AR66 removal on ZNa-P
a: X1X2, B: X1X3, c: X1X4 and d:X2X4

Furthermore, the design software employed in this study offers a better comprehensive analysis of the interaction effects between different factors on the adsorption capacity trough 3D surface plots and ANOVA results.

The ANOVA results, as outlined in **Table A2** in the appendix, indicates a quadratic relationship between the adsorption capacity of AR66 on ZNa-P and the selected variables, as expressed by Equation 25:

$$Y = 1417{,}4179 - 172{,}4882X_1 + 329{,}46637X_2 - 233{,}3188X_3 + 76{,}064205X_4 - 64{,}18888X_1X_2 + 19{,}689242X_1 + 16{,}30547X_1X_4 - 53{,}81246X_2X_3 + 13{,}798999X_2X_4 - 15{,}48413X_3X_4 - 3{,}847371X_1^2 - 63{,}69737X_2^2 + 24{,}142629X_3^2 - 7{,}405133X_4^2 \qquad \text{Eq. 25}$$

The results highlight the notable positive influence of the initial AR66 concentration and contact time on the adsorption capacity of AR66 on ZNa-P. Conversely, both pH and adsorbent amount exhibited negative effects. ANOVA results indicate that the most significant interactions are observed between pH and initial concentration followed by the interaction between initial concentration and adsorbent dosage. Additionally, positive effects were observed in the interactions between pH and adsorbent amount, pH and contact time, and initial concentration and contact time. Conversely, negative effects were observed in the interactions between pH and initial concentration, as well as initial concentration and adsorbent amount. However, the quadratic effects were deemed insignificant. Therefore, Equation 25 was simplified by excluding these insignificant parameters, resulting in the final CCD model equation:

$$Y = 1417{,}4179 - 172{,}4882\,X_1 + 329{,}46637\,X_2 - 233{,}3188\,X_3 + 76{,}064205\,X_4 - 64{,}18888\,X_1X_2 + 19{,}689242\,X_1 + 16{,}30547\,X_1X_4 - 53{,}81246\,X_2X_3 + 13{,}798999\,X_2X_4 - 15{,}48413X_3X_4 \qquad \textit{Eq. 26}$$

The value of the coefficient of determination slightly decreased when variables with low explanatory power were removed from the dependent variable, making the equation simpler.

Figure 8 depicts the interaction between pH and initial concentration at various levels of adsorbent mass and contact time. Increasing the initial concentration while simultaneously decreasing the pH significantly enhances the adsorption capacity of AR66 on ZNa-P. The combination of a lower pH and a high initial concentration contributes to the rapid elevation of the adsorption capacity on the ZNa-P surface. The nonlinear surface plots and the presence of curvatures in the 3D surface analysis confirm the ANOVA results [88].

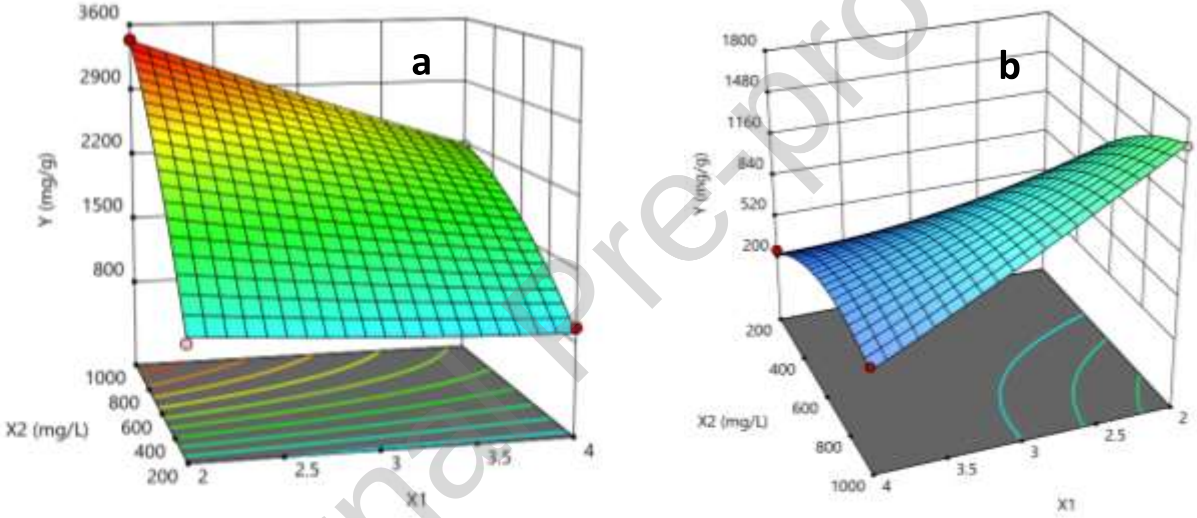

Figure 8. Response surfaces at constant adsorbent mass and contact time.
(a) 0.2g/L and 25 min (b) 1g/L and 5min

The combined influence of initial concentration and adsorbent mass is depicted in Figure 9 for constant pH and Contact time. The presence of curvatures in the plots demonstrates the strong interaction between initial concentration and adsorbent mass. The 3D plots illustrate that, at a constant pH and contact time, the highest adsorption capacities are attained when the initial concentration and adsorbent mass are near their respective 1 and -1 levels.

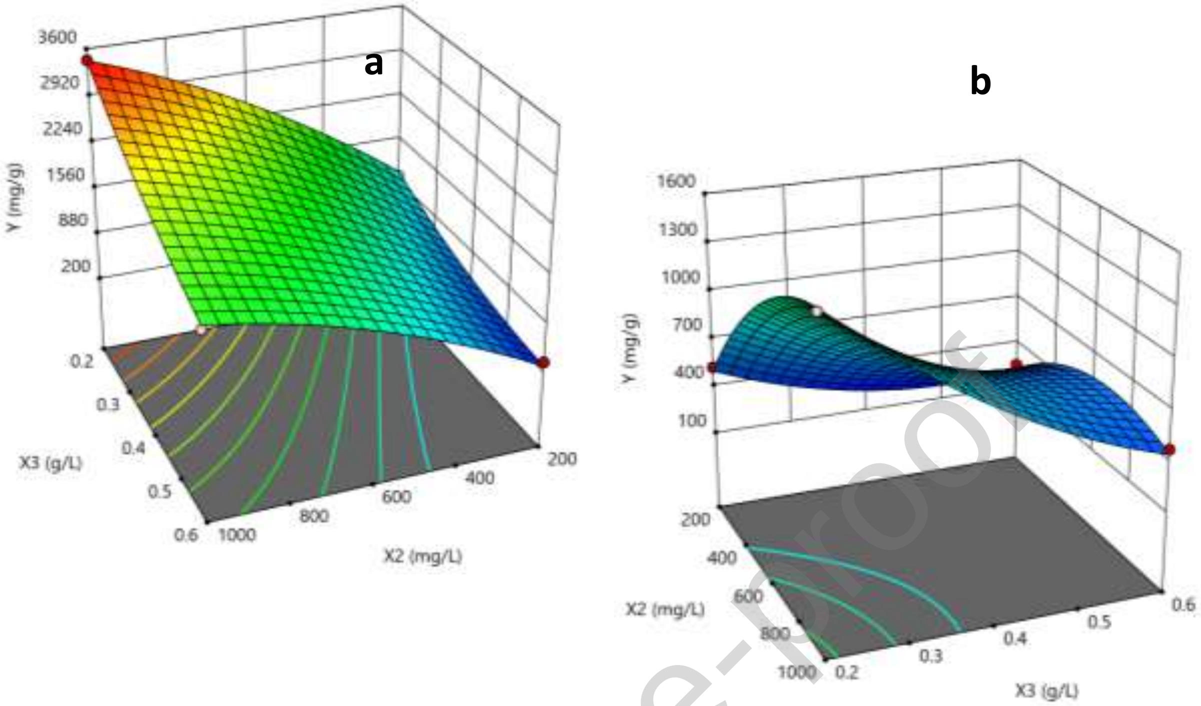

Figure 9. Response surface at constant pH and contact time
(a) 2 and 25min, (b) 4 and 5min

The joint effects of the remaining quadratic terms (X_1X_3, X_1X_4, X_2X_4, X_3X_4) on the adsorption capacity were found to be relatively insignificant with F-values lower than 10. The interaction impacts of pH-mass of adsorbent, pH-contact time, initial concentration-contact time, and mass of adsorbent-contact time are displayed in 3D response surface plots in Figure A1. The results show that the interaction effects involving contact time were the least significant. The contour lines appeared more linear, and the colored sections were almost parallel to the contact time axes, indicating a minimal influence of contact time on the response. The effect of contact time became more noticeable at higher concentrations.

The model equation generated by the design software provides a concise representation of the individual and combined effects of the model terms, as indicated by their respective coefficients. Positive coefficients signify a positive impact on the response, while negative coefficients suggest unfavorable effects. The numerical values of the coefficients reflect the relative influence of the corresponding terms on the response, aligning well with the observations from the surface response plots.

3.4. Kinetics of adsorption

Figure 10 presents the adsorption capacities of AR66 on ZNa-P over time, at various initial dye concentrations. The graph indicates that for lower concentrations ($C_0 < 500$ mg/L), the adsorption process was rapid, with equilibrium being achieved within the first few minutes ($t < 5$ min). At higher concentrations, more than 85% of the dye was adsorbed during an initial phase of adsorption (10-20 min), followed by a gradual approach to equilibrium within approximately 30 minutes for a concentration of 1000 mg/L and 3 hours for 2000 mg/L.

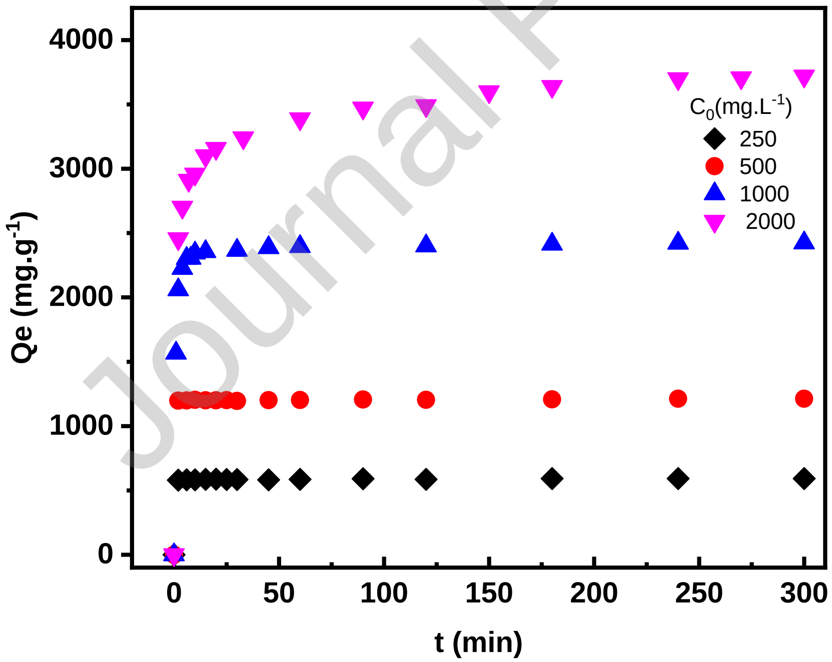

Figure 10. Effect of the contact time and the initial dye concentration on dye adsorption onto a ZNa-P, pH=3, m=0.4g.L^{-1} speed=250 rpm

3.5. Kinitics modeling

Table 4 displays the correlation coefficients and kinetic constants derived from various models fitted to the kinetics data. Plots illustrating these models fitted to the experimental data points are shown in Figure A.2 in the appendix. The models used in this analysis include the pseudo-first order, pseudo-second order, Elovich, diffusion-chemisorption model, Boyd, and intra-particle diffusion models.

The results indicate that the pseudo-first order plots yielded relatively low R^2 values ranging from 0.12 to 0.92. Furthermore, the calculated values of Q_e did not correspond with the observed experimental outcomes. These findings indicate that the adsorption process of the dye onto the zeolite did not adhere to a first-order reaction. However, the regression analysis based on the second-order model through the linear plot of t/Q_t versus t shown in Figure A.2 (b) exhibited satisfactory agreement between Q_e.cal values, obtained from the second-order model, and the experimentally determined values Q_e.exp. R^2 values for all initial dye concentrations are close to unity, signifying the model's precision in describing the adsorption kinetics and implying a chemisorption mechanism.

The Elovich model, shown in Figure A.2 c, did not exhibit clear straight lines, particularly for concentrations of 250, 500, and 1000 mg/L. The low values of coefficient of determination (R^2=0.287, 0.495, 0.726) suggest that the Elovich model does not accurately describe the adsorption of the dye on ZNa-P.

For the diffusion-chemisorption model shown in Figure A.2 (d), Table 4 shows that R^2 are close to 1 ($R^2 > 0.999$) for most initial dye concentrations. The Qe.cal values exhibit significant concurrence with the experimental data, particularly for the initial concentrations within the range of 250-1000 mg/L. These outcomes suggest that the adsorption of AR66 on ZNa-P can be accurately characterized by the diffusion-chemisorption model.

Table 4. Comparison of pseudo first order, pseudo second order, Elovich and Diffusion-Chemisorption models for AR66 adsorption on ZNa-P

C (mg. L^{-1})	250	500	1000	2000
Experimental data				
$Q_{exp}(mg.g^{-1})$	591,55	1213,10	2424,24	3707,91
Pseudo-first order model				
$k_1\ (min^{-1})$	0.015	0.011	0.019	0.022
$Q_e\ (mg.g^{-1})$	13.26	24.08	215.522	1460.40
R^2	0.442	0.3376	0.784	0.822
Pseudo-second order model				
$k_2\ (g.mg^{-1}min^{-1})$	0.0073	0.0045	7.59 10^{-4}	6.94 10^{-}
$Q_e(mg.g^{-1})$	587,48	1204,63	2435,06	^{5}3738,02
R^2	0.999	0.999	1	0.999
Elovich model				
$\alpha\ (mg.g^{-1}min^{-1})$	6.24 10^{18}	1.36 10^{18}	1.10 10^{11}	5.25 10^{6}
$\beta\ (g.mg^{-1})$	0.7513	0.3641	0.0105	0.0042
R^2	0.2877	0.4957	0.5783	0.9887
Diffusion-Chemisorption Model				
$Q_e(mg.g^{-1})$	591.72	1214.25	2498.79	3911.66
$K_{DC}(mg/g.min^{1/2})$	9085.54	23537.11	5632.38	3808.04
R^2	0.9999	0.9999	0.9992	0.9993

3.5.1. Intra-particle diffusion

The kinetics data were further evaluated using the intra-particle diffusion adsorption model, and the outcomes are illustrated in Figure 11. The corresponding model parameters and R^2 can be found in Table 5. Figure 11 reveals a multi-linearity pattern regardless of the initial dye concentration, suggesting the involvement of multiple steps in the adsorption process [89]. In the case of elevated concentrations (1000 mg/L and 2000 mg/L), three distinct linear regions are observed, whereas for lower concentrations (250 mg/L and 500 mg/L), only two regions are observed. The first stage, represented by the initial linear segment, occurs within the first three minutes and can be attributed to rapid external mass transfer followed by surface adsorption (film diffusion). In this phase, the pollutant is conveyed to the outer surface of the adsorbent. Subsequently, a gradual adsorption phase is observed exclusively for the higher concentrations, wherein intra-particle diffusion could potentially act as the rate-controlling step. Following approximately 15 minutes, the third phase commences, signifying the attainment of the final equilibrium stage. In this phase, intra-particle diffusion progressively decelerates due to saturation and the restricted accessibility of active sites.

For lower concentrations, the adsorption process appears to be very rapid during the initial stage, and the equilibrium region is quickly reached due to the low concentration of remaining dye. This suggests that, for low concentrations, adsorption mainly occurs in the first stage and may be limited to external surface adsorption, as there is a significant amount of active surface area compared to the dye quantity in the solution [10] [90]. As depicted in Figure 11, it is evident that the linear sections of the intermediate and final regions do not intersect at the origin. This observation suggests that intra-particle diffusion alone does not solely govern the rate-limiting step in the adsorption process.

Table 5. Intra-particle diffusion model parameters

Initial dye concentration (mg/L)	Kp_1 mg $g^{-1}min^{-0.5}$	Kp_2 mg g^{-1} $min^{-0.5}$	C_2	R^2	Kp_3 mg g^{-1} $min^{-0.5}$	C_3	R^2
250	846.79	/	/	/	0.683	580.82	0.717
500	1107.80	/	/	/	0.935	1196.14	0.773

1000	1736.48	384.34	1050.50	0.942	8.39	2298.19	0.792
2000	409.85	254.61	2158.63	0.931	43.87	3014.18	0.957

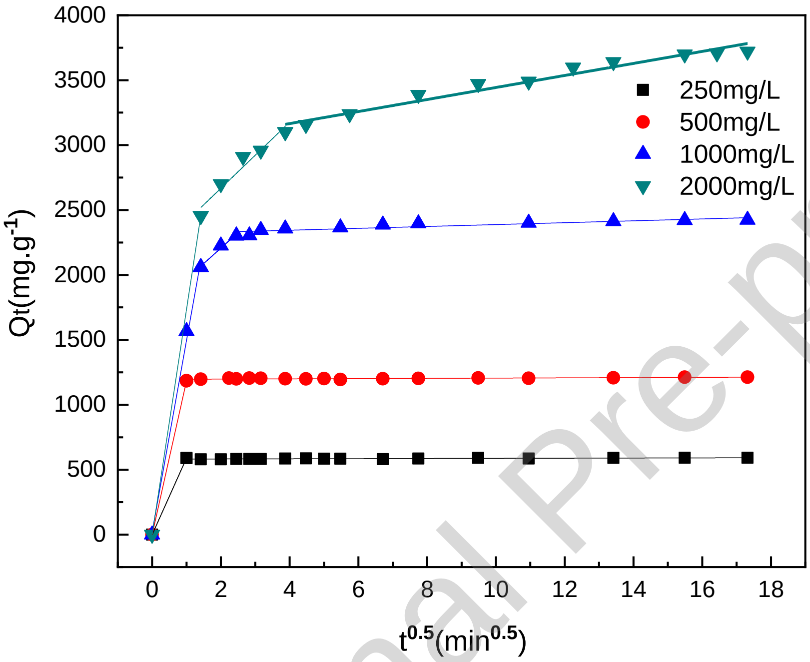

Figure 11. Kinetic simulation by the Intra-particle diffusion model for different initial concentration

3.6. Isotherms of adsorption

Figure 12 presents the isotherm depicting the adsorption of AR66 onto ZNa-P at room temperature (approximately 24°C). The storyline effectively demonstrates that as the concentration of the dye in the solution increases, there is a corresponding rise in the adsorption capacity until it reaches a saturation point, indicating a state of equilibrium. With an increase in the concentration of the solution, there is a proportional increase in the number of dye molecules being adsorbed onto the surface of the adsorbent. This continues until it reaches a maximum value, signifying that all the active sites on the adsorbent surface are fully utilized. Beyond this point, further increases in concentration do not lead to an increase in the quantity of adsorbed molecules. The utmost value denotes the highest capacity for adsorption. In the present investigation, an approximate estimation of the maximum adsorption capacity of AR66 on ZNa-P was recorded to be around 3700 mg/g.

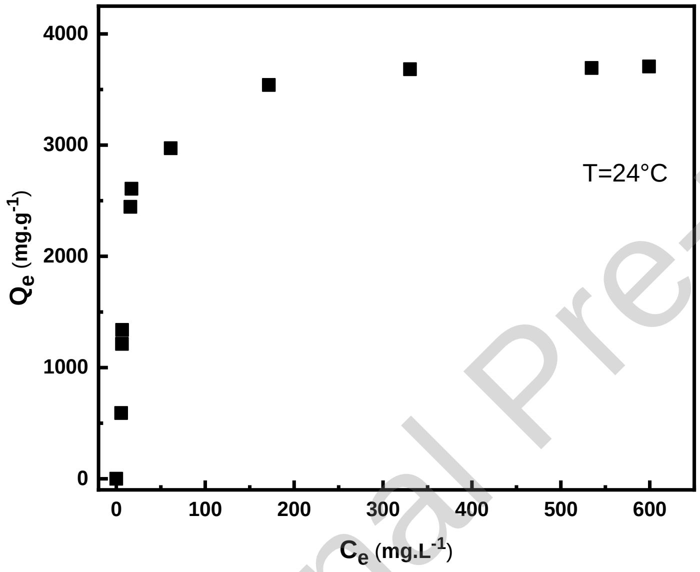

Figure 12. Experimental data (symbols) of experimental isotherm data m=0.4gL^{-1}, pH=3

3.6.1. Langmuir and Freundlich models

The experimental data from the isotherm analysis were evaluated using both Langmuir and Freundlich models. The resulting graphs are illustrated in Figure 13. The parameters obtained from these models are displayed in Table 6. It is evident that the Langmuir model exhibited a superior fit to the experimental data in comparison to the Freundlich model. This conclusion is supported by a higher coefficient of determination (R^2 = 0.957) and a notable concurrence between the calculated Qm and the experimental Qexp values. These findings suggest that the adsorption of AR66 onto ZNa-P follows a monolayer adsorption mechanism. The dimensionless separation factor (RL), calculated for the Langmuir model, was determined to be 0.006, falling within the favorable adsorption range of 0-1, further supporting the favorable nature of the adsorption process [58].

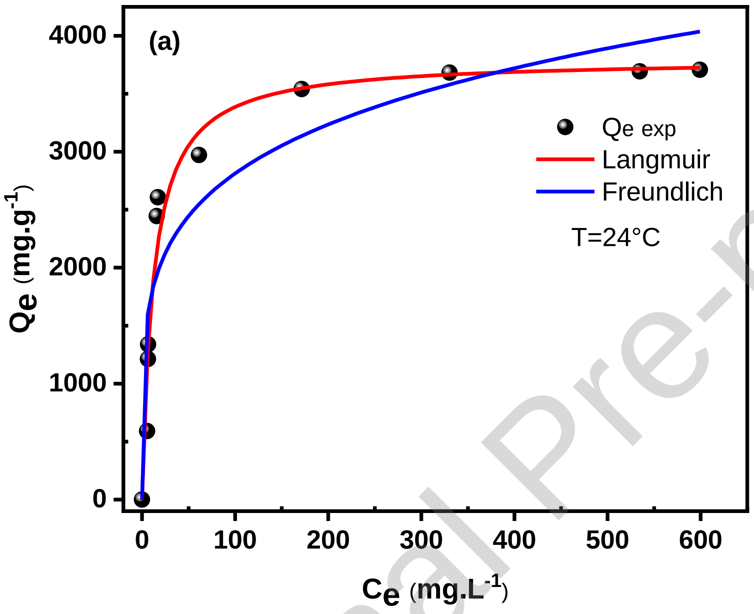

Figure 13. Experimental data (symbols) and nonlinear regression of experimental isotherm data obtained by means of the Langmuir, Freundlich models

3.6.2. Toth and Sips models

The experimental data from the isotherm analysis were subjected to analysis using the three-parameter Sips and Toth models, and the resulting plots are depicted in Figure 14. The parameters derived from fitting these models are summarized in Table 6. It is apparent that both the Sips and Toth models demonstrate a favorable fit to the experimental isotherm data, as evidenced by high R^2 values of 0.973 and 0.957 respectively. Additionally, these models yield

Q_m values that closely correspond to the experimental values. The results obtained from both models suggest that the adsorption system is heterogeneous in nature [61].

Table 6. Langmuir, Freundlich, Sips and Toth parameters for AR66 adsorptionon ZNa-P

Model	**parameter**	**24°C**
Experimental	q_m (mg. g^{-1})	3707.27
Langmuir	K_L (L. mg^{-1})	0.082
	q_m(mg. g^{-1})	3801.27
	R_L	0.006
	R^2	0.957
Freundlich	K_F (L. mg^{-1})	1110.30
	n	4.95
	R^2	0.855
Sips	K_S (L. mg^{-m})	0.097
	q_m(mg. g^{-1})	3595.79
	m	1.61
	R^2	0.973
Toth	K_T (mg. g^{-1})	3671.82
	a_T (L. mg^{-1})	14.10
	t	0.974
	R^2	0.957

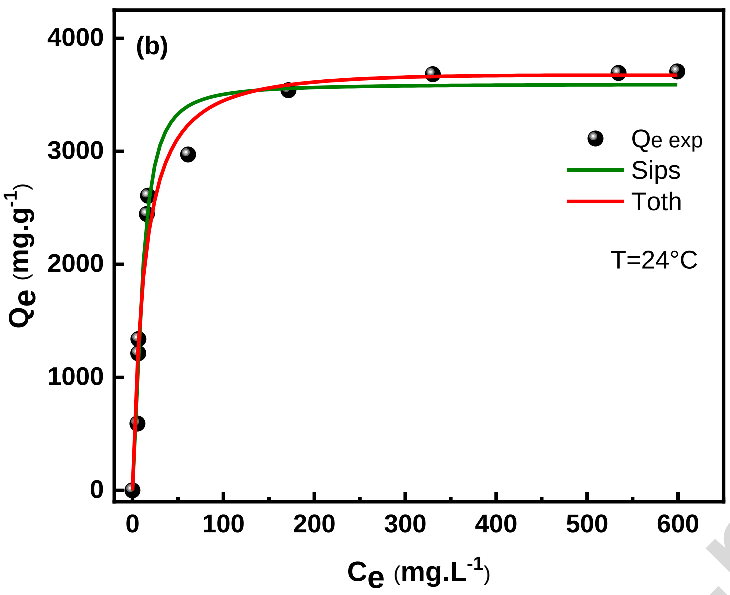

Figure 14. Experimental data (symbols) and nonlinear regression of experimental isotherm data obtained by means of the Sips and Thoth models

3.6.3. Effect of the Temperature and thermodynamic study

The adsorption process is significantly influenced by temperature, which is considered one of the most crucial parameters. The impact of temperature on the adsorption of AR66 onto ZNa-P is illustrated in Figure 15, indicating a slight decrease in the adsorption capacity as the operating temperature increases from 20°C to 40°C. The adsorption capacity decreases from approximately 3250 mg/g to 2990mg/g. This observation suggests that the adsorption of AR66 onto ZNa-P is favorable at lower temperatures, indicating an exothermic process. To gain a better understanding of the temperature's influence on the adsorption process, it is essential to determine the thermodynamic parameters. Through the utilization of Equations 27, 28 and 29 and plotting ln(K_c) against 1/T (see Figure A.3), several thermodynamic parameters such as the

Gibbs free energy change (ΔG°) in J/mol, enthalpy (ΔH°) in J/mol, and entropy (ΔS°) in J/K.mol can be determined. The evaluated parameters are summarized in Table 7.

$$\mathrm{Ln}(\rho K_c) = -\frac{1}{RT}\Delta H^{\circ} + \frac{1}{R}\Delta S^{\circ} \qquad \text{Eq. 27}$$

$$\left(K_c = \frac{Q_e}{C_e}\right) \qquad \text{Eq. 28}$$

$$\Delta G^{\circ} = \Delta H^{\circ} - T\Delta S^{\circ} \qquad \text{Eq. 29}$$

The determination of the equilibrium constant Kc (L/g) relies on the water density ρ (g/L), the gas constant R (8.314 J/mol.K), and the temperature T (K) of the solution. The negative value of the enthalpy, -9 kJ/mol (as shown in Table 7), confirms that the adsorption of AR66 onto ZNa-P is an exothermic process. A positive ΔS° indicates a strong attraction between the adsorbent and dye molecules, as well as an increase in disorder at the liquid/solid interface. Moreover, the adsorption process is spontaneous and thermodynamically feasible at all temperatures, as indicated by the negative ΔG°. Similar findings have been reported for the adsorption of anionic dyes such as Reactive Red 239 [91] and Congo Red onto zeolite [92].

Table 7. The thermodynamic parameters of AR66 adsorption onto ZNa-P

ΔH° (kJ/mol)	**ΔS°** **(J/K.mol)**	**ΔG° (kJ/mol)**		
		20°C	30°C	40°C
-9.035	39.47	-14.08	-14.76	-15.44

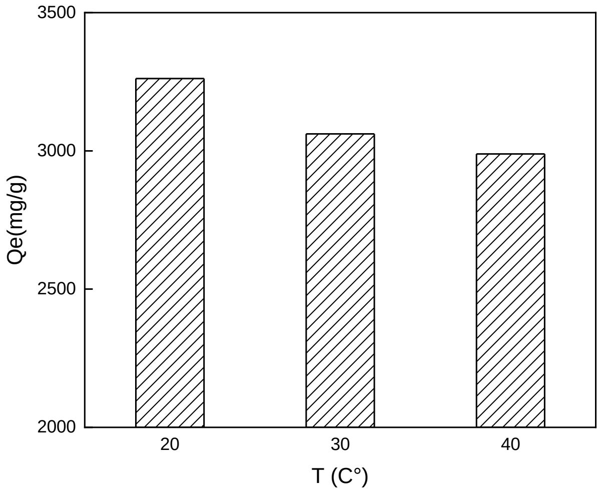

Figure 15. The effect of the temperature on the AR66 adsorption onto ZNa-P

3.7. Gaussian Process Regression coupled with Lévy flight distribution

Following the optimization of ten kernel functions using the LFD algorithm in combination with the base function, the most effective kernel function was chosen based on statistical criteria. The outcomes of this selection process are presented in Table 8, which provides details on the best model and its corresponding parameters (kernel scale and sigma). The table also includes the model's performance assessment using various statistical metrics (R, R^2, R^2_{adj}, RMSE, EPM, ESP, and MAE) for three distinct phases (training, validation, and all data), along with the kernel settings. Additionally, the table shows the preferred kernel function, the resulting basis functions, the count of Lévy flights utilized, and the number of iterations required to achieve the best model.

Table 8. Performances of the GPR-LFD model.

LFD	**Max_iteration=50** **SearchAgents_no=100**

	Kernel function	***Basis Function***	***Kernel Scale***		***Sigma***	**Quantile**	**R/R^2/R$^2_{adj}$**			**RMSE/EPM/ESP/MAE**		
			Sigma M	**Sigma F**			**Train**	**Val**	**ALL**	**Train**	**Val**	**ALL**
GPR_DA	***ARD-Exponential***	***Constant***	17.3259 8.6661 14.9219 61.4577	1396.1	88.0905	21	0.9989 0.9979 0.9974	0.9984 0.9969 0.9938	0.9988 0.9977 0.9974	34.8610 1.9008 2.9295 21.8034	39.3369 2.0435 2.4734 32.2020	36.2618 1.9436 2.7678 24.9230

Table 8 demonstrates strong correlation, high coefficient of determination and adjusted coefficient of determination, almost reaching 1, across all three phases. Conversely, the statistical coefficients obtained by the model for the three phases were notably low, confirming the model's precision. These results are presented in Figure A.4, providing a graphical representation of the findings.

3.8. Optimization and Validation of the optimum conditions

The Lévy flight distribution method was employed to optimize the independent parameters for achieving maximum AR66 uptake. The optimization results were subsequently validated through laboratory experiments using CCD and GPR_LFD. Table 9 presents the comparison between the predicted values and the experimental results, including the corresponding error between them.

Where: $$Error = Experimental\ response - Predicted\ response \qquad \text{Eq. 30}$$

Table 9. Comparison between actual and predicted responses at optimum conditions.

CCD	
• X_1 = 2. X_2 = 1000 mg/L. X_3= 0.2 g/L and X_4= 25 min	
AR66uptake (mg/g). experimental values	3437.88
AR66uptake (mg/g). predicted values	3642.8
Error	204.9200
GPR_LFD	
• X_1 = 2. X_2 = 1000 mg/L. X_3= 0.2 g/L and X_4= 25 min	
AR66uptake (mg/g). experimental values	3437.88
AR66uptake (mg/g). predicted values	3405.3
Error	32.5800

Based on the results provided in Table 9, it can be seen that the optimal conditions for AR66 absorption were determined to be $X_1 = 2, X_2 = 1000\ mg/L, X_3 = 0.2\ g/L, and\ X_4 = 25\ min$, according to both the CCD and GPR_LFD models. The laboratory validation of these conditions resulted in an absorption of 3437.88 mg/g of AR66. The CCD model predicted an absorption value of 3642.8 mg/g, while the GPR_LFD model predicted 3405.3 mg/g. The error between the experimental and predicted values was lower in the GPR_LFD model (32.5800 mg/g) compared to the CCD model (204.9200 mg/g), indicating the superior performance of the GPR_LFD model.

A user-friendly software application, specifically designed for Windows operating systems, has been developed to facilitate the optimization and prediction of AR66 adsorption quantities. This software application serves as a comprehensive tool that integrates the Central Composite Design

(CCD) and Gaussian Process Regression with Lévy Flight Distribution (GPR_LFD) methods, as illustrated in Figure 16.

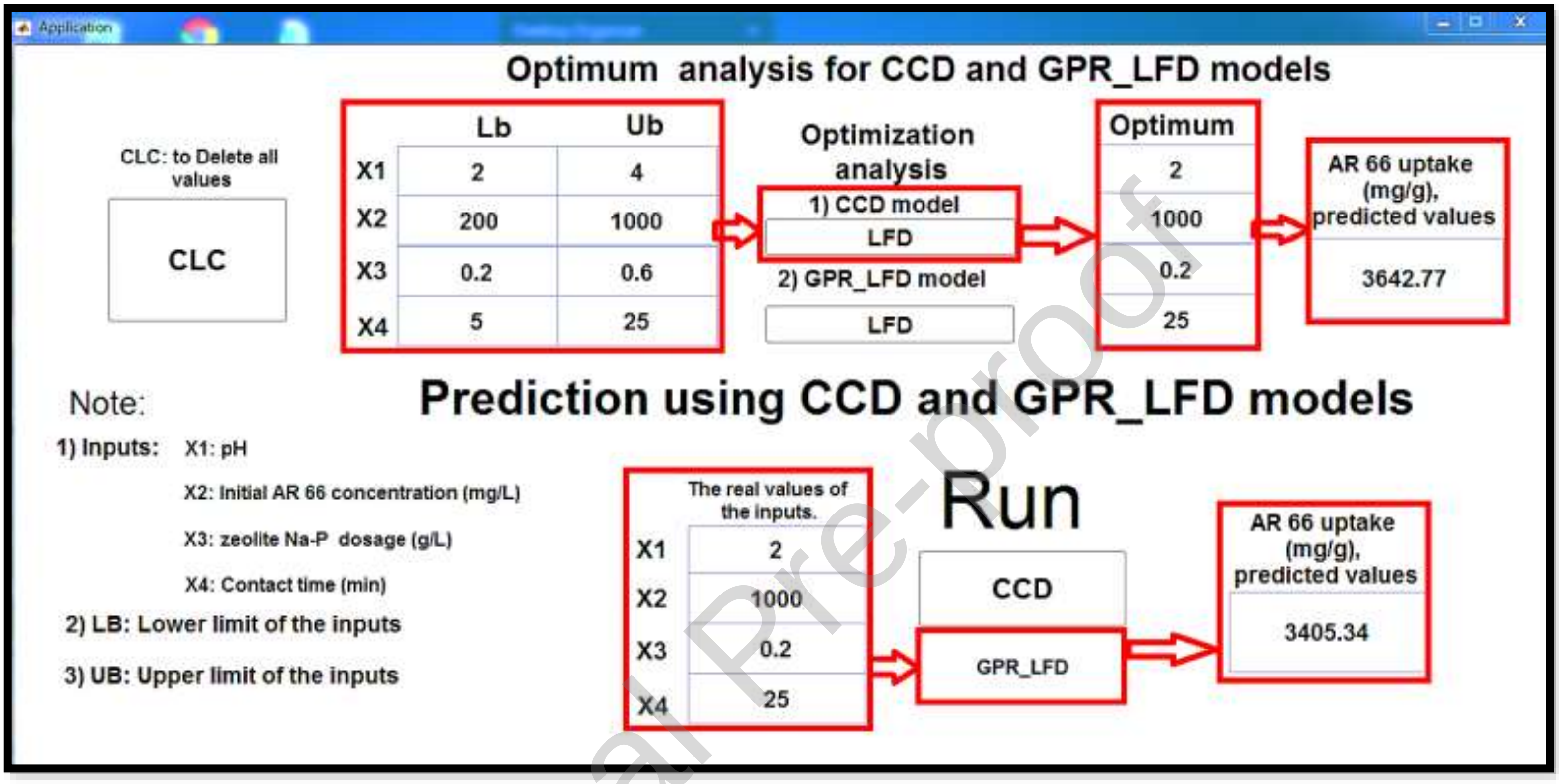

Optimum analysis for CCD and GPR_LFD models

CLC: to Delete all values

CLC

	Lb	Ub
X1	2	4
X2	200	1000
X3	0.2	0.6
X4	5	25

Optimization analysis

1) CCD model: LFD

2) GPR_LFD model: LFD

Optimum
2
1000
0.2
25

AR 66 uptake (mg/g), predicted values: 3642.77

Prediction using CCD and GPR_LFD models

Note:

1) Inputs: X1: pH
X2: Initial AR 66 concentration (mg/L)
X3: zeolite Na-P dosage (g/L)
X4: Contact time (min)

2) LB: Lower limit of the inputs

3) UB: Upper limit of the inputs

	The real values of the inputs.
X1	2
X2	1000
X3	0.2
X4	25

Run

CCD

GPR_LFD

AR 66 uptake (mg/g), predicted values: 3405.34

3.9.Figure 16. MATLAB Interface for optimization analysis using LFD and prediction of AR66 uptake using CCD and GPR_LFD.**Comparison of adsorption capacity with literature**

The primary purpose of Table 10 is to elucidate and enhance the understanding of the adsorption capacity of ZNa-P for AR66 by conducting a comprehensive comparison with other adsorbents documented in the existing literature. This table serves as a vital tool for evaluating the relative performance and effectiveness of ZNa-P in adsorbing AR66 in relation to various widely studied adsorbents. By presenting this detailed comparative analysis, Table 10 provides valuable insights into the exceptional potential and efficacy of ZNa-P as a superior adsorbent for AR66 removal, thereby making a notable contribution to the existing knowledge and understanding in this specific research domain.

Table 10. Comparison of AR66 adsorption capacity by different adsorbents.

Materials	**Adsorption capacity (mg/g)**	**References**
Acutodesmus obliquus strain	44.24	*[93]*
Fe_3O_4/natural zeolite	317.67	[94]
Calcined Mg–Al–CO_3	99.9	[95]
Mg-Cu-Al-Fe-CO_3	118	[10]
Calcined Mg-Cu-Al-Fe-CO_3	901	[10]
zeolite Na-P	3437.88	This work

The results presented in Table 10 provide valuable insights into the adsorption capacities of various materials, offering a comparative analysis of their performance in adsorbing AR66 (measured in mg/g).

- Acutodesmus obliquus strain demonstrates a relatively low adsorption capacity of 44.24 mg/g. This suggests that this particular material may have limited effectiveness in adsorbing AR66.
- Fe3O4/natural zeolite exhibits a moderate adsorption capacity of 317.67 mg/g. Although higher than Acutodesmus obliquus strain, it is still surpassed by other materials in the table.
- Calcined Mg-Al-CO3 displays a modest adsorption capacity of 99.9 mg/g. This indicates that its effectiveness in adsorbing AR66 is relatively low compared to other materials in the study.

- Mg-Cu-Al-Fe-CO3 demonstrates a slightly higher adsorption capacity of 118 mg/g, suggesting improved performance compared to Calcined Mg-Al-CO3.
- Calcined Mg-Cu-Al-Fe-CO3 shows a significant enhancement in adsorption capacity, reaching 901 mg/g. This substantial improvement indicates that the calcination process has a positive impact on the material's adsorption capabilities.
- Notably, zeolite Na-P stands out with an impressive adsorption capacity of 3437.88 mg/g. This exceptionally high value highlights the superior performance of zeolite Na-P in adsorbing AR66, making it the most effective adsorbent among the materials examined.

These results demonstrate the remarkable potential of zeolite Na-P as a highly efficient adsorbent for AR66 removal, surpassing the other materials in terms of adsorption capacity. The findings underscore the significance of zeolite Na-P as a promising candidate for effective water treatment applications involving the removal of AR66 contaminants.

4. Conclusion

This study focused on investigating the potential of using CFA transformed into zeolite (ZNa-P) as an adsorbent for the removal of AR66, an anionic dye, from wastewater. The characterization of CFA revealed its favorable characteristics for zeolite conversion. To optimize the process, RSM and GPR_LFD methods were employed to determine the optimal input parameters. The optimized conditions obtained for both CCD and GPR_LFD models included a pH of 2, an initial AR66 concentration of 1000 mg/L, an adsorbent dose of 0.2 g/L, and a contact time of 25 min. The CCD model predicted an adsorption value of 3642.8 mg/g, while the GPR_LFD model predicted 3405.3 mg/g. Experimental validation of these conditions in the laboratory resulted in an actual adsorption value of 3437.88 mg/g. Notably, the error obtained from the GPR_LFD model (32.58 mg/g) was lower than that from the CCD model (204.92 mg/g), indicating the superior performance of the GPR_LFD model. These findings highlight the effectiveness, accessibility, and cost-effectiveness of ZNa-P as an adsorbent with a high adsorption capacity for AR66.

5. Acknowledgements

This work is supported by the Algerian Ministry of Higher Education, the Ministry of Higher Education in Saudi Arabia and the Department of Physics, Faculty of Science, Taibah University, Madinah, Saudi Arabia. It is also supported in part by the Natural Sciences and Engineering Research Council of Canada (NSERC-CRD grant).

References

[1] H. Tahraoui, S. Toumi, A.H. Hassein-Bey, A. Bousselma, A.N.E.H. Sid, A.-E. Belhadj, Z. Triki, M. Kebir, A. Amrane, J. Zhang, Advancing Water Quality Research: K-Nearest Neighbor Coupled with the Improved Grey Wolf Optimizer Algorithm Model Unveils New Possibilities for Dry Residue Prediction, Water 15 (2023) 2631.

[2] T. Robinson, G. McMullan, R. Marchant, P. Nigam, Remediation of dyes in textile effluent: A critical review on current treatment technologies with a proposed alternative, Bioresour. Technol. 77 (2001) 247–255. https://doi.org/10.1016/S0960-8524(00)00080-8.

[3] H. Tahraoui, S. Toumi, M. Boudoukhani, N. Touzout, A.N.E.H. Sid, A. Amrane, A.-E. Belhadj, M. Hadjadj, Y. Laichi, M. Aboumustapha, Evaluating the Effectiveness of Coagulation–Flocculation Treatment Using Aluminum Sulfate on a Polluted Surface Water Source: A Year-Long Study, Water 16 (2024) 400.

[4] E. Akceylan, M. Bahadir, M. Yilmaz, Removal efficiency of a calix[4]arene-based polymer for water-soluble carcinogenic direct azo dyes and aromatic amines, J. Hazard. Mater. 162 (2009) 960–966. https://doi.org/10.1016/j.jhazmat.2008.05.127.

[5] E. Mijowska, W. Konicki, D. Moszynski, E. Mijowska, Adsorption of anionic azo-dyes from aqueous solutions onto graphene oxide : Equilibrium , kinetic and thermodynamic studies, J. Colloid Interface Sci. 496 (2017) 188–200. https://doi.org/10.1016/j.jcis.2017.02.031.

[6] F. Rafii, J.D. Hall, C.E. Cerniglia, Mutagenicity of Azo Dyes Used in Foods , Drugs and Cosmetics Before and After Reduction by Clostridium Species from the Human Intestinal Tract, 35 (1997) 897–901.

[7] Y.M. Slokar, A.M. Le Marechal, Methods of Decoloration of Textile Wastewaters, Dyes Pigments 37 (1998) 335–356.

[8] M. Abbasi, N.R. Asl, Sonochemical degradation of Basic Blue 41 dye assisted by nanoTiO2 and H2O2, J. Hazard. Mater. 153 (2008) 942–947. https://doi.org/10.1016/j.jhazmat.2007.09.045.

[9] E. Errais, J. Duplay, F. Darragi, I.M. Rabet, A. Aubert, F. Huber, G. Morvan, Efficient anionic dye adsorption on natural untreated clay : Kinetic study and thermodynamic parameters, Desalination 275 (2011) 74–81. https://doi.org/10.1016/j.desal.2011.02.031.

[10] I. Harizi, D. Chebli, A. Bouguettoucha, S. Rohani, A. Amrane, A New Mg–Al–Cu–Fe-LDH Composite to Enhance the Adsorption of Acid Red 66 Dye : Characterization , Kinetics and Isotherm Analysis, Arab. J. Sci. Eng. (2018). https://doi.org/10.1007/s13369-018-3526-2.

[11] I. Akin, G. Arslan, A. Tor, M. Ersoz, Y. Cengeloglu, Arsenic (V) removal from underground water by magnetic nanoparticles synthesized from waste red mud, J. Hazard. Mater. 235–236 (2012) 62–68. https://doi.org/10.1016/j.jhazmat.2012.06.024.

[12] R. William, R.G. Thiery, R.M. Schuller, J.J. Subway, ash : a review of the and proposed classification system with emphasis on environmental impacts, Environ. Geol. NOTES 96 (1981).

[13] J. Pizarro, C. Ximena, J. Sebastián, C. Ortizc, N. Patricio, H. Cid, R. Héctor, D. Barros, N. Belzile, Adsorption of Cu2+ on coal fly ash modified with functionalized mesoporous silica, Fuel 156 (2015) 96–102.

[14] I. Smirnova, J. Mamic, W. Arlt, Adsorption of Drugs on Silica Aerogels, Langmuir 19 (2013) 8521–8525.

[15] I. Humelnicu, B. Adriana, M.-E. Ignatc, V. Dulmana, The removal of Basic Blue 41 textile dye from aqueous solution by adsorption onto natural zeolitic tuff : Kinetics and thermodynamics, Process Saf. Environ. Prot. 105 (2016) 274–287. https://doi.org/10.1016/j.psep.2016.11.016.

[16] F. Goodarzi, Characteristics and composition of fly ash from Canadian coal-fired power plants, Fuel 85 (2006) 1418–1427. https://doi.org/10.1016/j.fuel.2005.11.022.

[17] J.D.C. Izidoro, D.A. Fungaro, J.E. Abbott, S. Wang, Synthesis of zeolites X and A from fly ashes for cadmium and zinc removal from aqueous solutions in single and binary ion systems, Fuel 103 (2013) 827–834. https://doi.org/10.1016/j.fuel.2012.07.060.

[18] N. Koshy, D.N. Singh, Fly ash zeolites for water treatment applications, J. Environ. Chem. Eng. 4 (2016) 1460–1472. https://doi.org/10.1016/j.jece.2016.02.002.

[19] A.M. Cardoso, M.B. Horn, L.S. Ferret, C.M.N. Azevedo, Integrated synthesis of zeolites 4A and Na – P1 using coal fly ash for application in the formulation of detergents and swine wastewater treatment, J. Hazard. Mater. 287 (2015) 69–77. https://doi.org/10.1016/j.jhazmat.2015.01.042.

[20] M. Ahmaruzzaman, A review on the utilization of fly ash, Prog. Energy Combust. Sci. 36 (2010) 327–363. https://doi.org/10.1016/j.pecs.2009.11.003.

[21] J. Dêdêcêk, S. Sklenak, C. Li, F. Gao, J. Brus, Q. Zhu, T. Tatsumi, Effect of Al/Si Substitutions and Silanol Nests on the Local Geometry of Si and Al Framework Sites in Silicone-Rich Zeolites: A Combined High Resolution 27Al and 29Si NMR and Density Functional Theory/Molecular Mechanics Study, J. Phys. Chem. C 113 (2009) 14454–14466.

[22] Y. Liu, G. Wang, L. Wang, X. Li, Q. Luo, P. Na, Zeolite P synthesis based on fly ash and its removal of Cu (II) and Ni (II) ions, Chin. J. Chem. Eng. (2018) 1–8. https://doi.org/10.1016/j.cjche.2018.03.032.

[23] R. Juan, S. Hernández, J.M. Andrés, C. Ruiz, Synthesis of granular zeolitic materials with high cation exchange capacity from agglomerated coal fly ash, Fuel 86 (2007) 1811–1821.

[24] V. Berkgaut, A. Singer, High capacity cation exchanger by hydrothermal zeolitization of coal fly ash, Appl. Clay Sci. 10 (1996) 369–378.

[25] N. Murayama, T. Takahashi, K. Shuku, H. Lee, J. Shibata, Effect of reaction temperature on hydrothermal syntheses of potassium type zeolites from coal fly ash, Process. Int. J. Miner. 87 (2008) 129–133.

[26] X. Querol, A. Alastuey, A. López-Soler, F. Plana, A Fast Method for Recycling Fly Ash: Microwave-Assisted Zeolite Synthesis, Environ. Sci. Technol. 31 (1997) 2527–2533.

[27] T. Aldahri, J. Behin, H. Kazemian, S. Rohani, Synthesis of zeolite Na-P from coal fly ash by thermo-sonochemical treatment, Fuel 182 (2016) 494–501. https://doi.org/10.1016/j.fuel.2016.06.019.

[28] K. Adavi, A. Amini, M. Latifi, J. Shabanian, J. Chaouki, Kinetic study of multiphase reactions under microwave irradiation: a mini-review, Front. Chem. Eng. 4 (2022) 1059160.
[29] K. Adavi, J. Shabanian, J. Chaouki, Temperature Distribution Assessment in Gas–Solid Reactive and Nonreactive Systems Heated by Microwaves, Ind. Eng. Chem. Res. 62 (2023) 9970–9982.
[30] T. Aldahri, J. Behin, H. Kazemian, S. Rohani, Effect of microwave irradiation on crystal growth of zeolitized coal fly ash with different solid / liquid ratios, Adv. Powder Technol. 28 (2017) 2865–2874. https://doi.org/10.1016/j.apt.2017.08.013.
[31] S.S. Bukhari, J. Behin, H. Kazemian, S. Rohani, A comparative study using direct hydrothermal and indirect fusion methods to produce zeolites from coal fly ash utilizing single-mode microwave energy, J. Mater. Sci. 49 (2014) 8261–8271. https://doi.org/10.1007/s10853-014-8535-2.
[32] M. Abbasi, M.M. Habibi, Optimization and characterization of Direct Blue 71 removal using nanocomposite of Chitosan-MWCNTs : Central composite design modeling, J. Taiwan Inst. Chem. Eng. 62 (2016) 112–121. https://doi.org/10.1016/j.jtice.2016.01.019.
[33] R. Tariq, M. Abatal, A. Bassam, Computational intelligence for empirical modeling and optimization of methylene blue adsorption phenomena using available local zeolites and clay of Morocco, J. Clean. Prod. 370 (2022) 133517.
[34] M. Dolatabadi, M. Mehrabpour, M. Esfandyari, S. Ahmadzadeh, Adsorption of tetracycline antibiotic onto modified zeolite: Experimental investigation and modeling, MethodsX 7 (2020) 100885.
[35] J. Abdi, M. Vossoughi, N.M. Mahmoodi, I. Alemzadeh, Synthesis of amine-modified zeolitic imidazolate framework-8, ultrasound-assisted dye removal and modeling, Ultrason. Sonochem. 39 (2017) 550–564.
[36] M. Vakili, A. Mojiri, T. Kindaichi, G. Cagnetta, J. Yuan, B. Wang, A.S. Giwa, Cross-linked chitosan/zeolite as a fixed-bed column for organic micropollutants removal from aqueous solution, optimization with RSM and artificial neural network, J. Environ. Manage. 250 (2019) 109434.
[37] J.L. Fagundez, M.S. Netto, G.L. Dotto, N.P. Salau, A new method of developing ANN-isotherm hybrid models for the determination of thermodynamic parameters in the adsorption of ions Ag+, Co2+ and Cu2+ onto zeolites ZSM-5, HY, and 4A, J. Environ. Chem. Eng. 9 (2021) 106126.
[38] R.A. Rahman, O.A. Moamen, N. Abdelmonem, I.M. Ismail, Optimizing the removal of strontium and cesium ions from binary solutions on magnetic nano-zeolite using response surface methodology (RSM) and artificial neural network (ANN), Environ. Res. 173 (2019) 397–410.
[39] M. Sukumar, A. Sivasamy, G. Swaminathan, In situ biodecolorization kinetics of Acid Red 66 in aqueous solutions by Trametes versicolor, J. Hazard. Mater. 167 (2009) 660–663.
[40] N. Bouchelkia, H. Tahraoui, A. Amrane, H. Belkacemi, J.-C. Bollinger, A. Bouzaza, A. Zoukel, J. Zhang, L. Mouni, Jujube stones based highly efficient activated carbon for methylene blue adsorption: kinetics and isotherms modeling, thermodynamics and mechanism study, optimization via Response surface methodology and machine learning approaches, Process Saf. Environ. Prot. (2022).
[41] S. Farch, M.M. Yahoum, S. Toumi, H. Tahraoui, S. Lefnaoui, M. Kebir, M. Zamouche, A. Amrane, J. Zhang, A. Hadadi, L. Mouni, Application of Walnut Shell Biowaste as an Inexpensive Adsorbent for Methylene Blue Dye: Isotherms, Kinetics, Thermodynamics, and Modeling, Separations 10 (2023) 60. https://doi.org/10.3390/separations10010060.
[42] A. Imessaoudene, S. Cheikh, A. Hadadi, N. Hamri, J.-C. Bollinger, A. Amrane, H. Tahraoui, A. Manseri, L. Mouni, Adsorption Performance of Zeolite for the Removal of Congo Red Dye: Factorial Design Experiments, Kinetic, and Equilibrium Studies, Separations 10 (2023) 57.
[43] M. Kebir, H. Tahraoui, M. Chabani, M. Trari, N. Noureddine, A.A. Assadi, A. Amrane, N. Ben Hamadi, L. Khezami, Water Cleaning by a Continuous Fixed-Bed Column for Cr (VI) Eco-Adsorption with Green Adsorbent-Based Biomass: An Experimental Modeling Study, Processes 11 (2023) 363.

[44] N. Hamri, A. Imessaoudene, A. Hadadi, S. Cheikh, A. Boukerroui, J.-C. Bollinger, A. Amrane, H. Tahraoui, H.N. Tran, A.O. Ezzat, Enhanced Adsorption Capacity of Methylene Blue Dye onto Kaolin through Acid Treatment: Batch Adsorption and Machine Learning Studies, Water 16 (2024) 243.

[45] M. Batool, M.A. Abbas, I.A. Khan, M.Z. Khan, M. Saleem, A.U. Khan, K.M. Deen, M. Batool, A.L. Khan, S. Zhu, Response Surface Methodology Modeling Correlation of Polymer Composite Carbon Nanotubes/Chitosan Nanofiltration Membranes for Water Desalination, ACS EST Water 3 (2023) 1406–1421.

[46] M. Kebir, I. kahina Benramdhan, N. Noureddine, H. Tahraoui, B. Nadia, B. Houssine, A. Rachid, J. Zhang, A.A. ASSADI, L. Mouni, Sunlight Degradation and Mineralization of Food Dye Photoinduced by Homogenous Photo Fenton Fe (III) and Fe (II)/Complex: Surface Response Modeling, (2023).

[47] H. Tahraoui, A.-E. Belhadj, Z. Triki, N.R. Boudella, S. Seder, A. Amrane, J. Zhang, N. Moula, A. Tifoura, R. Ferhat, A. Bousselma, N. Mihoubi, Mixed Coagulant-flocculant Optimization for Pharmaceutical Effluent Pretreatment Using Response Surface Methodology and Gaussian Process Regression, Process Saf. Environ. Prot. (2022) S0957582022010102. https://doi.org/10.1016/j.psep.2022.11.045.

[48] M. Nedjhioui, N. Nasrallah, M. Kebir, H. Tahraoui, R. Bouallouche, A.A. Assadi, A. Amrane, B. Jaouadi, J. Zhang, L. Mouni, Designing an Efficient Surfactant–Polymer–Oil–Electrolyte System: A Multi-Objective Optimization Study, Processes 11 (2023) 1314.

[49] H. Tahraoui, A.-E. Belhadj, N. Moula, S. Bouranene, A. Amrane, Optimisation and Prediction of the Coagulant Dose for the Elimination of Organic Micropollutants Based on Turbidity, Kem. U Ind. 70 (2021) 675–691.

[50] S. Lagergren, B.K. Svenska, About the theory of so-called adsorption of soluble substances, K. Sven. Vetenskapsakademiens Handl. 24 (1898) 1–39.

[51] Y.-S. Ho, G. Mckay, The Kinetics of Sorption of Divalent Metal Ions Onto Sphagnum Moss Peat, Water Res. 34 (2000) 735–742.

[52] C. Djama, A. Bouguettoucha, D. Chebli, A. Amrane, H. Tahraoui, J. Zhang, L. Mouni, Experimental and Theoretical Study of Methylene Blue Adsorption on a New Raw Material, Cynara scolymus—A Statistical Physics Assessment, Sustainability 15 (2023) 10364. https://doi.org/10.3390/su151310364.

[53] S. Roginsky, Y.B. Zeldovich, The catalytic oxidation of carbon monoxide on manganese dioxide, Acta Physi Chem USSR 1 (1934) 554.

[54] OzkanAksakal, HandanUcun, Equilibrium, kinetic and thermodynamic studies of the biosorption of textile dye (Reactive Red 195) onto Pinus sylvestris L, J. Hazard. Mater. 181 (2010) 666–672.

[55] A. Guediri, A. Bouguettoucha, H. Tahraoui, D. Chebli, J. Zhang, A. Amrane, L. Khezami, A.A. Assadi, The Enhanced Adsorption Capacity of Ziziphus jujuba Stones Modified with Ortho-Phosphoric Acid for Organic Dye Removal: A Gaussian Process Regression Approach, Water 16 (2024) 1208.

[56] A. Guediri, A. Bouguettoucha, H. Tahraoui, D. Chebli, A. Amrane, J. Zhang, Thermodynamic study and the development of a support vector machine model for predicting adsorption behavior of orange peel-derived beads in wastewater treatment, J. Mol. Liq. (2024) 124860.

[57] C. Sutherland, C. Venkobachar, A diffusion-chemisorption kinetic model for simulating biosorption using forest macro-fungus, fomes fasciatus, Int. Res. J. Plant Sci. 1 (2010) 107–117.

[58] W.J. Weber Jr, J.C. Morris, Kinetics of adsorption on carbon from solution, J. Sanit. Eng. Div. Am. Soc. Civ. Eng. 89 (1963) 31–60.

[59] Y. Guo, Z. Zhu, Y. Qiu, J. Zhao, Enhanced adsorption of acid brown 14 dye on calcined Mg/Fe layered double hydroxide with memory effect, Chem. Eng. J. 219 (2013) 69–77. https://doi.org/10.1016/j.cej.2012.12.084.

[60] K.R. Hall, L.C. Eagleton, A. Acrivos, T. Vermeulen, Pore- and Solid-Diffusion Kinetics in Fixed-Bed Adsorption under Constant-Pattern Conditions, Ind. Eng. Chem. Fundam. 5 (1966) 212–223. https://doi.org/10.1021/i160018a011.

[61] K.Y. Foo, B.H. Hameed, Insights into the modeling of adsorption isotherm systems, Chem. Eng. J. 156 (2010) 2–10. https://doi.org/10.1016/j.cej.2009.09.013.

[62] H. Tahraoui, A.-E. Belhadj, A. Amrane, E.H. Houssein, Predicting the concentration of sulfate using machine learning methods, Earth Sci. Inform. 15 (2022) 1023–1044. https://doi.org/10.1007/s12145-022-00785-9.

[63] E.H. Houssein, M.R. Saad, F.A. Hashim, H. Shaban, M. Hassaballah, Lévy flight distribution: A new metaheuristic algorithm for solving engineering optimization problems, Eng. Appl. Artif. Intell. 94 (2020) 103731.

[64] H. Moussa, F. Dahmoune, M. Hentabli, H. Remini, L. Mouni, Optimization of ultrasound-assisted extraction of phenolic-saponin content from Carthamus caeruleus L. rhizome and predictive model based on support vector regression optimized by dragonfly algorithm, Chemom. Intell. Lab. Syst. 222 (2022) 104493.

[65] G.K. Khiam, R.R. Karri, N.M. Mubarak, M. Khalid, R. Walvekar, E.C. Abdullah, M.E. Rahman, Modelling and optimization for methylene blue adsorption using graphene oxide/chitosan composites via artificial neural network-particle swarm optimization, Mater. Today Chem. 24 (2022) 100946.

[66] A. Azari, M.H. Mahmoudian, M.H. Niari, I. Eş, E. Dehganifard, A. Kiani, A. Javid, H. Azari, Y. Fakhri, A.M. Khaneghah, Rapid and efficient ultrasonic assisted adsorption of diethyl phthalate onto FeIIFe2IIIO4@ GO: ANN-GA and RSM-DF modeling, isotherm, kinetic and mechanism study, Microchem. J. 150 (2019) 104144.

[67] A. Bousselma, D. Abdessemed, H. Tahraoui, A. Amrane, Artificial Intelligence and Mathematical Modelling of the Drying Kinetics of Pre-treated Whole Apricots, Kem. U Ind. 70 (2021) 651–667.

[68] A. Hadadi, A. Imessaoudene, J.-C. Bollinger, A. Bouzaza, A. Amrane, H. Tahraoui, L. Mouni, Aleppo pine seeds (Pinus halepensis Mill.) as a promising novel green coagulant for the removal of Congo red dye: Optimization via machine learning algorithm, J. Environ. Manage. 331 (2023) 117286.

[69] H. Tahraoui, S. Toumi, A.H. Hassein-Bey, A. Bousselma, A.N.E.H. Sid, A.-E. Belhadj, Z. Triki, M. Kebir, A. Amrane, J. Zhang, Advancing Water Quality Research: K-Nearest Neighbor Coupled with the Improved Grey Wolf Optimizer Algorithm Model Unveils New Possibilities for Dry Residue Prediction, Water 15 (2023) 2631.

[70] H. Tahraoui, A.-E. Belhadj, A. Amrane, E.H. Houssein, Predicting the concentration of sulfate using machine learning methods, Earth Sci. Inform. (2022) 1–22.

[71] H. Tahraoui, A. Amrane, A.-E. Belhadj, J. Zhang, Modeling the organic matter of water using the decision tree coupled with bootstrap aggregated and least-squares boosting, Environ. Technol. Innov. 27 (2022) 102419.

[72] H. Tahraoui, A.-E. Belhadj, A.-E. Hamitouche, M. Bouhedda, A. Amrane, Predicting the concentration of sulfate (So4 2–) in drinking water using artificial neural networks: A case study: Médéa-algeria, Desalination Water Treat. 217 (2021) 181–194.

[73] H. Tahraoui, A.E. Belhadj, A.E. Hamitouche, Prediction of the Bicarbonate Amount in Drinking Water in the Region of Médéa Using Artificial Neural Network Modelling, Kem. U Ind. 69 (2020) 595–602. https://doi.org/10.15255/KUI.2020.002.

[74] M.M. Yahoum, S. Toumi, S. Hentabli, H. Tahraoui, S. Lefnaoui, A. Hadjsadok, A. Amrane, M. Kebir, N. Moula, A.A. Assadi, Experimental Analysis and Neural Network Modeling of the Rheological Behavior of Xanthan Gum and Its Derivatives, Materials 16 (2023) 2565.

[75] M. Zamouche, M. Chermat, Z. Kermiche, H. Tahraoui, M. Kebir, J.-C. Bollinger, A. Amrane, L. Mouni, Predictive Model Based on K-Nearest Neighbor Coupled with the Gray Wolf Optimizer

Algorithm (KNN_GWO) for Estimating the Amount of Phenol Adsorption on Powdered Activated Carbon, Water 15 (2023) 493.

[76] M. Zamouche, H. Tahraoui, Z. Laggoun, S. Mechati, R. Chemchmi, M.I. Kanjal, A. Amrane, A. Hadadi, L. Mouni, Optimization and Prediction of Stability of Emulsified Liquid Membrane (ELM): Artificial Neural Network, Processes 11 (2023) 364.

[77] H. Tahraoui, A.E. Belhadj, A.E. Hamitouche, Prediction of the Bicarbonate Amount in Drinking Water in the Region of Médéa Using Artificial Neural Network Modelling, Kem. U Ind. 69 (2020) 595–602. https://doi.org/10.15255/KUI.2020.002.

[78] H. Tahraoui, A.-E. Belhadj, A. Hamitouche, M. Bouhedda, A. Amrane, Predicting the concentration of sulfate (SO42–) in drinking water using artificial neural networks: a case study: Médéa-Algeria, Desalination Water Treat. (2021) 14.

[79] H. Tahraoui, A. Amrane, A.-E. Belhadj, J. Zhang, Modeling the organic matter of water using the decision tree coupled with bootstrap aggregated and least-squares boosting, Environ. Technol. Innov. 27 (2022) 102419. https://doi.org/10.1016/j.eti.2022.102419.

[80] H. Tahraoui, A.-E. Belhadj, A. Hamitouche, M. Bouhedda, A. Amrane, Predicting the concentration of sulfate (SO42-) in drinking water using artificial neural networks: a case study: Médéa-Algeria, DESALINATION WATER Treat. 217 (2021) 181–194. https://doi.org/10.5004/dwt.2021.26813.

[81] H. Tahraoui, A.E. Belhadj, A.E. Hamitouche, Prediction of the Bicarbonate Amount in Drinking Water in the Region of Médéa Using Artificial Neural Network Modelling, Kem. U Ind. 69 (2020) 595–602. https://doi.org/10.15255/KUI.2020.002.

[82] A. Bousselma, D. Abdessemed, H. Tahraoui, A. Amrane, Artificial Intelligence and Mathematical Modelling of the Drying Kinetics of Pre-treated Whole Apricots, Kem. U Ind. (2021). https://doi.org/10.15255/KUI.2020.079.

[83] M. Park, C.L. Choi, W.T. Lim, M.C. Kim, J. Choi, N.H. Heo, Molten-salt method for the synthesis of zeolitic materials II. Characterization of zeolitic materials, Microporous Mesoporous Mater. 37 (2000) 91–98. https://doi.org/10.1016/S1387-1811(99)00195-X.

[84] E.M. Flanigen, H. Khatami, H.A. Szymanski, Molecular Sieve Zeolites Advances in Chemistry Series, Am. Chem. Soc. Wash. DC 101 (1971) 201.

[85] X. Zhang, Q. Guo, Z. Zhang, F. Ling, W. Sun, R. Li, Synthesis and characterization of Y/B Ccomposite zeolite and its hydrocraking performance, in: Sayari Abdelhamid, J. Mietek (Eds.), Nanoporous Mater. - Proc. 5th Int. Symp., 2008: pp. 99–108.

[86] T. Al-dahri, A.A. Abdulrazak, I.H. Khalaf, S. Rohani, Response surface modeling of the removal of methyl orange dye from its aqueous solution using two types of zeolite synthesized from coal fly ash, (2018). https://doi.org/10.1166/mex.2018.1433.

[87] M. Kousha, S. Tavakoli, E. Daneshvar, A. Vazirzadeh, A. Bhatnagar, Central composite design optimization of Acid Blue 25 dye biosorption using shrimp shell biomass, J. Mol. Liq. 207 (2015) 266–273. https://doi.org/10.1016/j.molliq.2015.03.046.

[88] R. Manivasagan, P. Karthic, Application of Response Surface Methodology for the Extraction of Chromium(VI) by Emulsion Liquid Membrane, J. Taiwan Inst. Chem. Eng. 41 (2010) 105–110.

[89] W.H. Cheung, Y.S. Szeto, G. Mckay, Intraparticle diffusion processes during acid dye adsorption onto chitosan, Bioresour. Technol. 98 (2007) 2897–2904. https://doi.org/10.1016/j.biortech.2006.09.045.

[90] R. Morais, R. Gabriel, L. Gonçalves, V. Regina, L. Constantino, C. Valentim, P. Damasceno, J. Tronto, F. Garcia, Adsorption of Acid Yellow 42 dye on calcined layered double hydroxide : Effect of time , concentration , pH and temperature, Appl. Clay Sci. 140 (2017) 132–139. https://doi.org/10.1016/j.clay.2017.02.005.

[91] E. Alver, A. ü Metin, Anionic dye removal from aqueous solutions using modified zeolite: Adsorption kinetics and isotherm studies, Chem. Eng. J. 200–202 (2012) 59–67. https://doi.org/10.1016/j.cej.2012.06.038.
[92] I. Harizi, T. Aldahri, D. Chebli, S. Rohani, A. Bouguettoucha, Highly Efficient Adsorbent for Anionic Dye using a Synthesized Zeolite P from Coal Fly Ash, in: ISERD 142nd Int. Conf., Stockholm, Sweden, 2018: pp. 1–6.
[93] P. Sarwa, R. Vijayakumar, S.K. Verma, Adsorption of acid red 66 dye from aqueous solution by green microalgae Acutodesmus obliquus strain PSV2 isolated from an industrial polluted site, Open Access Libr. J. 1 (2014) 1–8.
[94] A.A. AbdulRazak, Z.M. Shakor, S. Rohani, Optimizing Biebrich Scarlet removal from water by magnetic zeolite 13X using response surface method, J. Environ. Chem. Eng. 6 (2018) 6175–6183.
[95] D. Chebli, A. Bouguettoucha, A. Reffas, C. Tiar, M. Boutahala, H. Gulyas, A. Amrane, Removal of the anionic dye Biebrich scarlet from water by adsorption to calcined and non-calcined Mg–Al layered double hydroxides, Desalination Water Treat. 57 (2016) 22061–22073.

Supplementary Material

Table A1. Experimental design based on CCD used in this study

Run	X_1	X_2	X_3	X_4	Y	Predicted Y
	pH	(mg/L)	(g/L)	(min)	(mg/g)	(mg/g)
1	2.5	600	0.4	15	1746.21	1586,59
2	3	600	0.4	20	1580.68	1486,56
3	3	600	0.4	15	1499.55	1417,40
4	2	200	0.6	25	334.75	287,12
5	2	200	0.2	25	995.08	1069,22
6	4	1000	0.2	5	1540.91	1536,00
7	2	1000	0.2	5	3034.85	3029,59
8	3	600	0.4	15	1298.55	1417,40
9	2	1000	0.6	25	1759.85	1796,55
10	4	1000	0.2	25	2174.24	2206,94
11	4	200	0.2	25	943.18	863,53
12	3	600	0.4	15	1456.89	1417,40
13	3	600	0.4	15	1389.36	1417,40
14	2	1000	0.6	5	1613.26	1634,24
15	4	200	0.6	5	248.36	194,05
16	4	1000	0.6	25	903.03	878,87
17	2	1000	0.2	25	3437.88	3439,65
18	2	200	0.6	5	323.23	345,60
19	3	600	0.4	10	1206.52	1333,44

20	3.5	600	0.4	15	1121.59	1240,53
21	3	400	0.4	15	977.65	1024,70
22	3	600	0.3	15	1714.39	1674,35
23	3	600	0.5	15	1209.39	1208,74
24	4	200	0.2	5	523.64	548,13
25	3	600	0.4	15	1378.03	1417,40
26	4	1000	0.6	5	474.747	455,67
27	3	600	0.4	15	1403.03	1417,40
28	3	800	0.4	15	1770.45	1682,71
29	2	200	0.2	5	908.33	879,95
30	4	200	0.6	25	336.14	396,46

Table A2. ANOVA of the BBD for the optimization of the elimination of AR66

Term	**Estimation**	**Standard error**	**t ratio**	**Prob. > |t|**
Linear				
Constant	1417,4179	25,55942	55,46	<,0001*
X1	-172,4882	11,95225	-14,43	<,0001*
X2	329,46637	11,95225	27,57	<,0001*
X3	-233,3188	11,95225	-19,52	<,0001*
X4	76,064205	11,73466	6,48	<,0001*
Interaction				
X1*X2	-64,18888	6,089457	-10,54	<,0001*
X1*X3	19,689242	6,089457	3,23	0,0056*
X2*X3	-53,81246	6,089457	-8,84	<,0001*
X1*X4	16,30547	6,161323	2,65	0,0183*
X2*X4	13,798999	6,161323	2,24	0,0407*
X3*X4	-15,48413	6,161323	-2,51	0,0239*
Quadratic				
X1*X1	-3,847371	54,55648	-0,07	0,9447
X2*X2	-63,69737	54,55648	-1,17	0,2612
X3*X3	24,142629	54,55648	0,44	0,6644
X4*X4	-7,405133	36,88008	-0,20	0,8436
Regression results	**R=0.9958; R^2=0.9916; RMSE=92.212**			

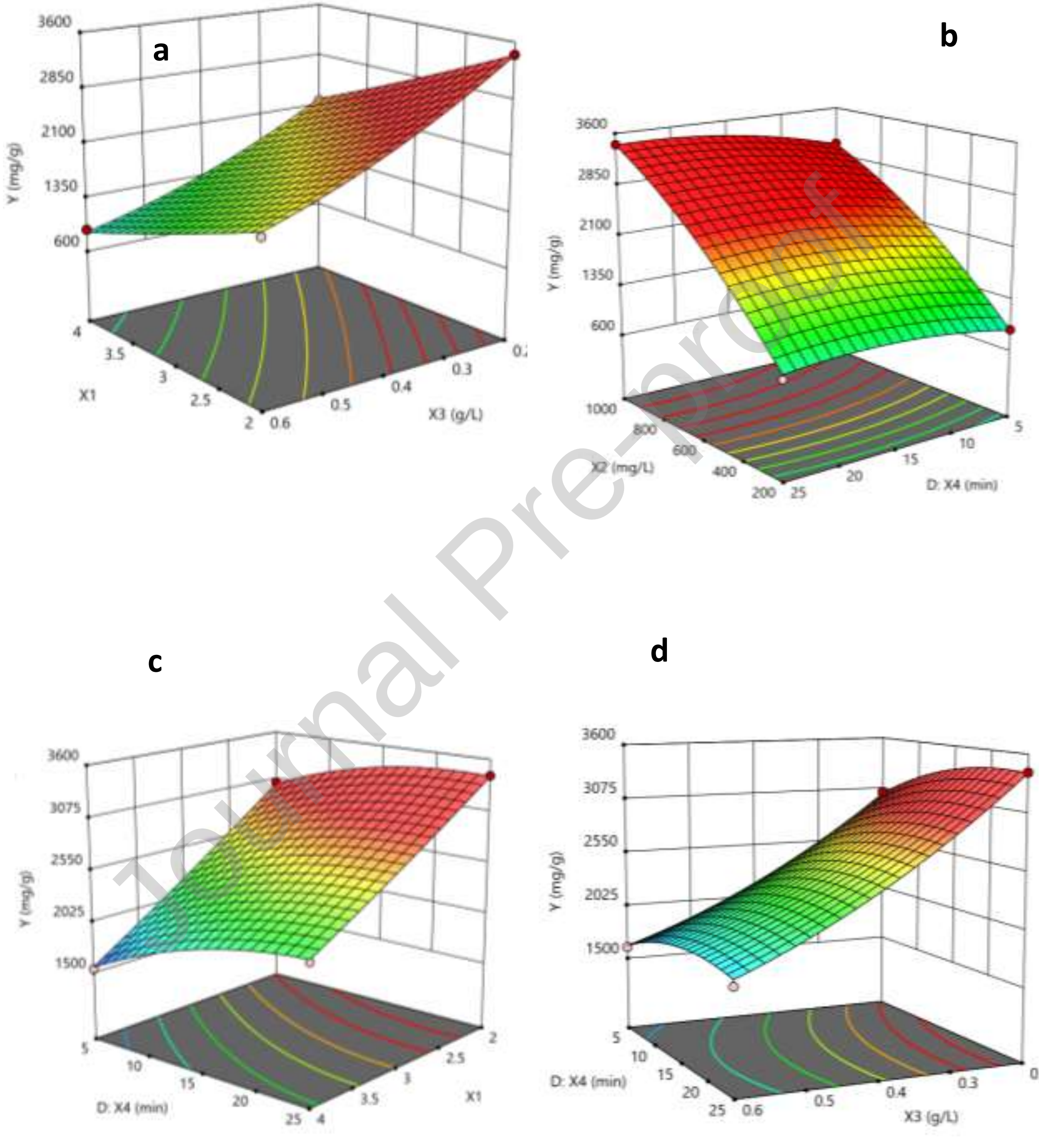

Figure A.1 The interaction effect of: (a) pH - adsorbent mass X_1X_3(b) initial concentration-contact time X_2X_4 (c) pH -contact time X_1X_4 (d) adsorbent mass-contact time X_3X_4

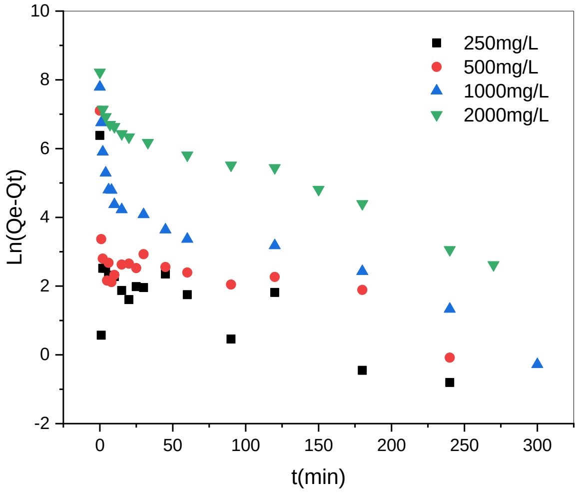
Ln(Qe-Qt)
t(min)
250mg/L
500mg/L
1000mg/L
2000mg/L
-2
0
2
4
6
8
10
0
50
100
150
200
250
300

(a)

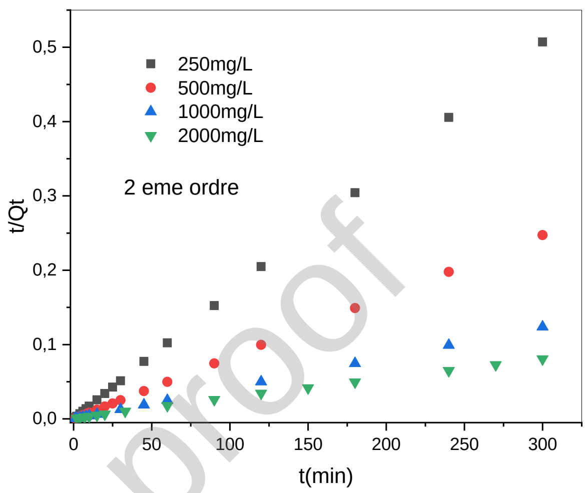
t/Qt
t(min)
250mg/L
500mg/L
1000mg/L
2000mg/L
2 eme ordre
0,0
0,1
0,2
0,3
0,4
0,5
0
50
100
150
200
250
300

(b)

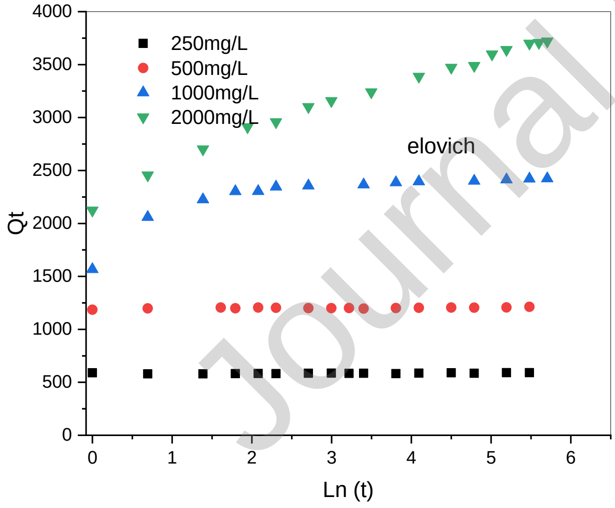
Qt
Ln (t)
250mg/L
500mg/L
1000mg/L
2000mg/L
elovich
0
500
1000
1500
2000
2500
3000
3500
4000
0
1
2
3
4
5
6

(c)

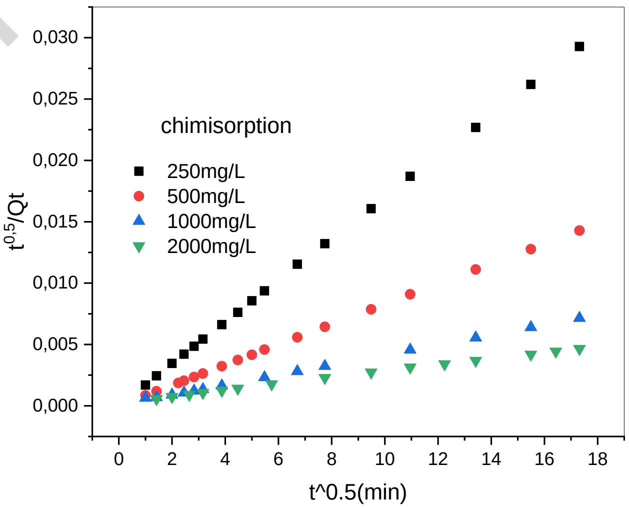
t^{0,5}/Qt
t^0.5(min)
chimisorption
250mg/L
500mg/L
1000mg/L
2000mg/L
0,000
0,005
0,010
0,015
0,020
0,025
0,030
0
2
4
6
8
10
12
14
16
18

(d)

Figure A.2 Kinetics of AR66 adsorption onto ZNa-P fitted to (a) pseudo first order (b) pseudo second order (c) Elovich and (d) diffusion chemisorption model

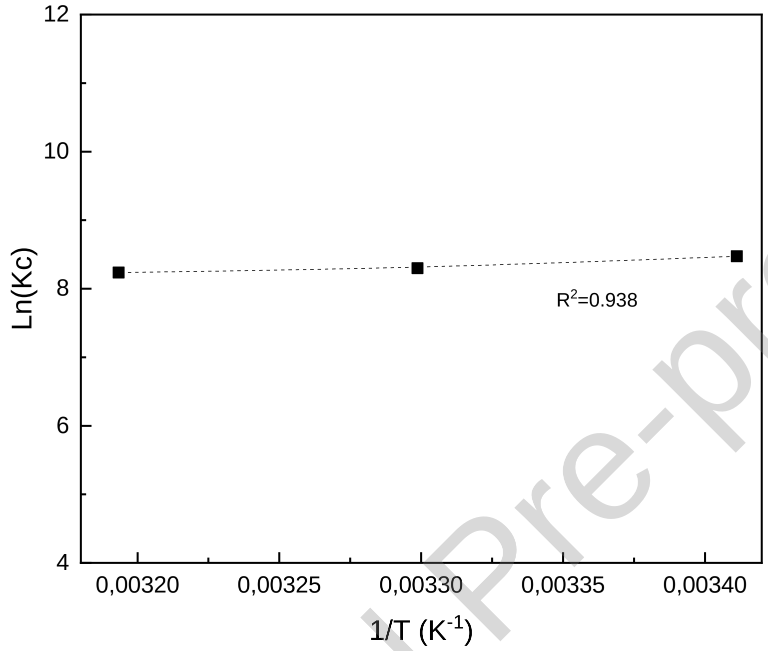

Figure A.3. The effect of the temperature on the AR66 adsorption onto ZNa-P

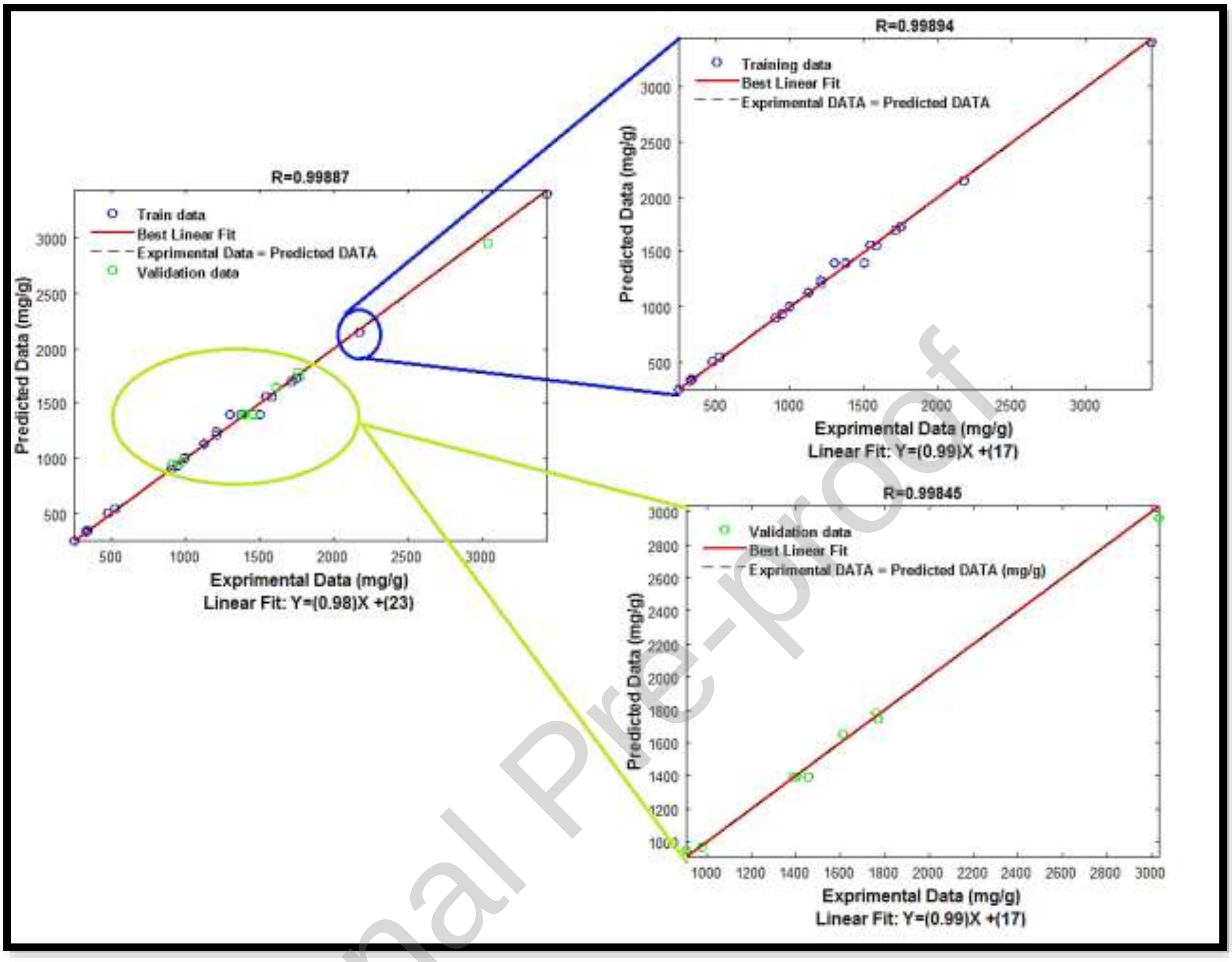

Figure A.4 Relationship between the experimental and the GPR-LFD model predicted values

Declaration of interests

The authors declare that they have no known competing financial interests or personal relationships that could have appeared to influence the work reported in this paper.

HIGHLIGHTS

- Adsorption of Acid red 66 dye onto Zeolite Na-P Synthesized from Waste Coal Fly Ash.
- Optimization of AR66 adsorption using the Central Composite Design (CCD).
- Database created by the CCD is modeled using the Gaussian Process Regression (GPR).
- The GPR is coupled with with Lévy flight distribution algorithm (LFD).
- Superior adsorption of AR66 is achieved with the GPR_ LFD model.